Lewis

s. 2nd
Office,

1. *Ref.*
ent, *J.*
982.
grain
986.
ram).
1965.
ssiles
emo,

CHAPTER 4

Solid Propellant Combustion and Internal Ballistics of Motors

BERNADETTE GOSSANT*

1. Introduction

The understanding and complete control of combustion are critical areas of research when seeking better performance for solid propellant rocket motors. The purpose of this chapter is to present the current knowledge in internal ballistics of solid propellant rocket motors. Its first part deals with the description of experimental determinations of the burning rate, necessary for any internal ballistics calculations. A description of the combustion of the various propellant ingredients follows. The last two sections of this chapter are devoted to the combustion analysis under actual steady-state or unsteady operation conditions of the rocket motor.

2. Solid Propellant Combustion

2.1. BURNING RATE

2.1.1. Background

The combustion of a solid propellant is characterized by the way its surface regresses once it has begun to burn. The burning rate is the distance traveled by the flame front per unit of time, measured normally to the burning surface. This front is assumed to be regular and, in most cases, progresses in a direction normal to itself. This has been experimentally verified (within the

*With the participation of Paul Tchepidjian.

precision limit of burnt profile measurements) by interrupting the propellant combustion and examining the surface.

The burning rate versus pressure law is usually expressed by the formula given by Saint Robert and Vieille:

$$r = ap^n \tag{1}$$

where:

n is the pressure exponent;
a is the rate of burning constant.

For a given propellant and a pressure ranging from 3 to 15 MPa, the pressure exponent takes a typical value between 0.2 and 0.7. Some propellants, however, have a different behavior: their pressure exponent is zero (the so-called plateau effect), or even negative (mesa effect). The coefficient a in eqn (1) is known to be dependent on the initial or in-depth temperature of the propellant. An established empirical law is:

$$a = a_0 \exp[\sigma_p(T_i - T_i^0)] \tag{2}$$

where:

T_i^0 = an initial reference temperature;
T_i = the initial propellant temperature;
a_0 = the burning rate constant at T_i^0;
a = the burning rate constant at T_i;

$$\sigma_p = \left(\frac{\partial \ln r}{\partial T_i}\right)_p \left\{\begin{array}{l}\text{Sensitivity of the burning rate at initial}\\ \text{temperature under constant pressure. As a first}\\ \text{approximation this coefficient may be considered as a}\\ \text{constant.}\end{array}\right.$$

Finally, under certain extreme conditions (violent shock, explosion), the burning rate may considerably increase and become greater than the speed of sound. This catastrophic condition is called a detonation and is not discussed in this chapter.

Tailoring a propellant will always include as major objective to minimize the values of pressure exponent and temperature coefficient (Chapter 1), while ensuring that its mechanical properties will still be sufficient for future applications. There are a large number of physicochemical parameters affecting the burning rate. They will be analyzed in detail when combustion mechanisms of the main propellant families are described.

2.1.2. Experimental determination of the burning rate

Several methods are used. Some of these methods require very small amounts of propellant, and are therefore preferred when performing preliminary analyses. The values obtained must later be confirmed at larger scale (control propellant grains).

2.1.2.1. *The strand burner method*

In this method a small sample (standard size) of propellant is fired in a bomb at constant pressure. This method has many advantages, including low cost and quick-and-easy implementation. A disadvantage is that the reduced size of the propellant sample may exaggerate the dependence on propellant inhomogeneities.

(a) Preparation of the samples

The samples used are strands, with a square section (10×10 or 5×5 mm^2) approximately 170 mm long. They are inhibited along their whole length to ensure that combustion occurs perpendicular to the surface. The type of inhibitor depends on the propellant composition. Each strand is perforated with four holes:

- the first hole, close to one end, is used to place the ignition wire;
- the other three, placed at 20, 85 and 150 mm respectively, are used to introduce lead wires which, by melting, allow the electrical detection of location of the flame front with time.

The samples are then placed vertically in a closed vessel, called a firing bomb.

(b) The firing bomb

The firing bomb currently used is made of steel (Fig. 1); its useful volume is 750 cm^3. A preliminary pressurization is done, usually with nitrogen; the test pressure level is kept constant during the combustion of the strand. Firings at various temperatures are made possible with the use of glycol or oil baths (for respectively low and high temperatures).

(c) Determination of the burning rate

The burning rate is obtained by knowing the burning distance as well as the burning time between two lead wires. These lead wires, acting as fuses, trigger a chronometer. As there are two strands per sample holder, four determinations of burning rate are done per test.

2.1.2.2. *Liquid strand burner method [1]*

This method also uses propellant strands. The strands, however, are shorter (68 mm) and are only equipped with an ignition wire. The firing

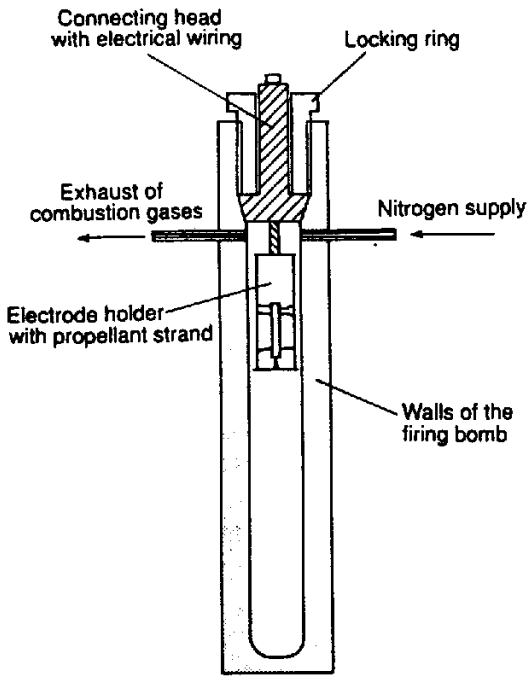

FIG. 4.1. Schematic of a strand burner firing bomb.

bomb is filled with water to ensure lateral restriction of the strand. It is then pressurized to a desired pressure level, using nitrogen. This level, however, is not regulated during firing.

The burning rate is obtained by knowing the strand useful length and the duration of the firing. The latter is determined by monitoring the noise made by combustion. The advantage of this method is that a preliminary lateral restriction of the strand is not necessary.

2.1.2.3. Ultrasonic method [2]

(a) Principle of the method

A mechanical wave is produced by an ultrasonic transducer which works either as transmitter or receiver. The ultrasonic wave travels through the propellant sample and is reflected on the burning surface. Because there is a tremendous difference in acoustic impedance between the propellant grain and its burning products, it is possible to deduce the unburnt propellant thickness by measuring the elapsed time between transmission and reception of the wave. To avoid wave attenuation, the maximum propellant grain thickness is 40 mm; the wave travel time is on the order of a few tens of microseconds. Changes in the thickness can therefore be monitored by transmitting periodic ultrasonic pulses during firing. Instantaneous values of the steady-state burning rate are obtained by derivation once the recorded signals have been decoded.

(b) Test firing rocket motor

This experimental device consists of a small rocket motor in which a cylindrical, "end-burning" sample of propellant (86 mm in diameter) is mounted. For technical reasons (measurements of small thicknesses, thermal insulation), a material with a similar acoustic impedance, called coupling material, is placed between the receiver (transmission frequency 5–25 MHz) and the propellant grain.

(c) Advantage of the method

This method allows the performance of direct, localized, and instantaneous measurements. Only a small amount of material is used, and a large portion of the burning rate law is obtained from just one firing. The pressure evolution inside the combustion chamber is obtained either through the geometry of the propellant grain, or by using eroding throats. However, the coupling material needs to be tailored to each family of propellant.

2.1.2.4. Standard ballistics test motors

These motors, used to verify the burning rate laws of the various propellant families, are characterized by a low evolution of the grain burning surface. As a result the firing may be done at practically constant pressure, which greatly simplifies results analysis.

Star-shaped or slotted tube propellant grains, used to measure the specific impulse, are discussed in their corresponding implementation in Chapter 3. Some propellant compositions require burning rate measurements to be done through end-burning grains ("cigarette-burning" combustion type). Table 1 provides an overview of the main characteristics of the various SNPE test motors.

The effective burning time t_{ce} is calculated from the pressure-time plot (Chapter 3). Similarly, the same iterative procedure is applied to the burning surface evolution curve versus the burnt propellant thickness; it gives:

- The "effective" surface area S_e;
- The "effective" burned web e_b, such as:

$$\int_0^{e_f} S(e) \cdot de = S_e \cdot e_b$$

where e_f is the propellant web thickness.

TABLE 1 *Main control propellant grains used at SNPE*

Grain designation	Star grains		Internal burning tube grain				End-burning grain		
	Mimosa	Campanule	Bates 3"5	Bates 7"	Bates 12"	32 × 16	Flora	Phlox	Panisse
Outer diameter (mm)	203	90	90	177.8	304.8	32	157	90	100
Diameter of propellant (mm)	198	86	86	167.6	298.4	32	151	85	90
Length of propellant (mm)	500	298	157	304.8	508.0	125	100	90	90
Diameter of star wedge (mm)	113.5	50.3	/	/	/	/			
Diameter of central port (mm)	/	/	60	116.8	203.2	16			
Propellant volume (cm^3)	12000	1340	470	3460	19000	75	1790	510	570
Effective web thickness (mm)	43.6	18.6	13.0	25.4	47.6	8	560	90	90

The calculation of the average burning rate is deduced:

$$r = \frac{e_b}{t_{ce}}$$

2.2. COMBUSTION MECHANISMS

Except for the ignition phase, the combustion of a solid propellant is a self-sustained phenomenon. Due to the heat feedback from the flame, the temperature rise of the propellant located very close to the surface causes its decomposition (structure changes, rupture of chemical bonds). Gaseous and reactive chemical products are released, in turn feeding the combustion in the flame zone.

2.2.1. Description of the burning zone

Study of the burning zone takes into account, in addition to the flame zone, the thin propellant layer close to the surface area where the temperature is raised. Propellant is a poor heat conductor, and since the flame is very close to the surface, the zone affected by combustion is very small. It is a few hundreds of microns thick.

2.2.1.1. Description of the phenomenon in the solid material

With a uniaxial assumption, the integration of the steady-state heat equation, including the following boundary conditions:

$$x = 0^- \qquad T = T_s$$

$$x = -\infty \qquad T = T_i, \qquad \frac{dT}{dx} = 0$$

gives the evolution of the temperature gradient in the steady-state regime (origin of the axis on the burning surface as it moves). It is expressed by the equation:

$$T = T_i + (T_s - T_i)\exp\left(\frac{r}{d_p}x\right) \tag{3}$$

where:

r = burning rate of the propellant;
T_i = initial temperature of the propellant, far from the burning surface;
T_s = surface temperature of propellant;
d_p = propellant heat diffusivity.

(a) Decomposition in the solid phase

The following analysis does not take into account the chemical reactions, thermally enhanced, occurring inside the propellant; those are endothermic (decomposition of polymer chains) or exothermic (recombination in the condensed phase of the chemical products resulting from the decomposition). But temperature profiles recorded with very fine thermocouples on homogeneous propellant samples [3] reasonably validate eqn (3). Lengellé *et al.* [4] demonstrated that decomposition reactions practically occur only at the surface.

(b) Kinetics of propellant grain decomposition: pyrolysis laws

- Composite propellants
  Experience demonstrates that, for the steady-state regime, the regressive burning rate r_i of each ingredient is related to the surface temperature:

$$r_i = A_i \exp\left(-\frac{E_i}{RT_{s,i}}\right) \tag{4}$$

where:

A_i = constant;
E_i = activation energy decomposition reactions;
$T_{s,i}$ = surface temperature;
R = universal gas constant;
i = stands for each propellant ingredient.

- Homogeneous propellants:
  The integration of the conservation equation for the non-decomposed propellant mass, assuming a zero-order reaction, gives:

$$r = \int_{-\infty}^{0} B_i \exp\left(\frac{E_p}{RT}\right) dx$$

where:

B_p = constant;
E_p = activation energy of the propellant decomposition reactions.

Taking into account the small thickness where reactions occur, Lengellé [5] shows that:

$$r = \exp\left(-\frac{E_p}{2RT_s}\right)\left\{\frac{B_p d_p}{\varepsilon_p}\left[1 - \frac{T_i}{T_s} - \frac{Q_s}{2c_p T_s}\right]\right\}^{1/2} \tag{15}$$

where:

d_p = propellant thermal diffusivity;

$\varepsilon_p = \dfrac{E_p}{RT_s}$;

T_i = initial temperature;
T_s = surface temperature;
Q_s = heat released by reactions in the solid phase (breakdown of the N-NO_2 chemical bonds and the reaction NO_2 + aldehyde in the condensed phase);
c_p = propellant specific heat.

Experiments validate this relationship for this kind of propellant [4].

2.2.1.2. *Description of the phenomenon in the gas*

Simplified, we may consider that the flame provides sufficient heat flux to maintain the regression of the solid propellant surface through the gaseous layer where the products released by reaction decompositions are hot, although still inactive. In a one-dimensional assumption, resolving the heat equation and assuming boundary conditions:

$$x = 0^+ \qquad T = T_s$$

$$x = x_f^- \qquad T = T_f, \qquad \lambda \left.\frac{dT}{dx}\right|_{x_f^-} = \dot{m} Q_F$$

we obtain the following temperature profile:

$$T = T_f + (T_f - T_s)\left[\exp\frac{\dot{m} c_g x}{\lambda_g} - \exp\frac{\dot{m} c_g x_f}{\lambda_g}\right] \Big/ \left[\exp\frac{\dot{m} c_g x_f}{\lambda_g} - 1\right] \tag{6}$$

where:

T_s = propellant surface temperature;
T_f = adiabatic temperature of the flame;
x_f = flame height;
$\dot{m}$ = mass flow rate of the gaseous reactive products;
c_g = specific heat of the gases, at constant pressure (assumed to be constant);
λ_g = heat conductivity of the gases, assumed to be constant;
Q_F = heat released by the flame.

The value of the flame heat flux (in $x = x_f^-$) allows the computation of the surface temperature T_s:

$$T_s = T_f - \frac{Q_F}{c_g}\left[\exp\frac{\dot{m} c_g x_f}{\lambda_g} - 1\right] \Big/ \exp\frac{\dot{m} c_g x_f}{\lambda_g} \tag{7}$$

Flame system

Kuo [6] presented a synthesis of the knowledge in this field. We will limit ourselves to pointing out that there are two major types of flames that must be considered when studying the combustion of propellants: laminar premixed flames, and laminar diffusion flames.

(a) Laminar premixed flames

In this case the molecules of the reactants are intimately mixed together. The flame height is completely controlled by the kinetics of chemical reactions.

$$x_f = x_r \simeq \frac{\dot{m}}{p^{\delta-2}} B_f \exp\left(-\frac{E_f}{RT}\right) \tag{8}$$

where:

δ = order of the chemical reaction;
x_r = height of the reaction;
E_f = activation energy of the reaction;
B_f = pre-exponential factor of the reaction;
p = combustion pressure.

(b) Laminar diffusion flames

Fuel and oxidizer are this time initially separated. The flame height, depending mainly on the diffusion of the products, needed before any chemical reaction, consists of two terms:

$$x_f = x_d + x_r \tag{9}$$

- x_r is the reaction height of the flame due to the intervention of kinetics after the products issued from decomposition have been mixed.
- x_d is this part of the total height which depends on the diffusion; it is estimated from Burke-Schumann analysis [7]. This analysis deals with the case of a Bunsen burner with two separate jets. It is applied by analogy to the case of the reactions between oxidizing products coming from the decomposition of ammonium perchlorate and combustible products coming from the decomposition of the binder. In this section we mention the equation for short flames which allows correlation of analysis and experience [8].

2.2.1.3. *Energetic balance at surface*

Continuing to assume that the reactions in condensed phase occur at the level of the burning surface, we have:

$$\lambda_g \left.\frac{dT}{dx}\right|_{0^+} = \lambda_p \left.\frac{dT}{dx}\right|_{0^-} + \dot{m} Q_s \tag{10}$$

where:

λ_g, λ_p = respectively, heat conductivity of the gas and of the propellant;
$\dot{m}$ = mass flow rate resulting from combustion;
Q_s = energy representing the total reactions at the surface; this value is negative if the final result is exothermic.

Therefore, using tiny thermocouples to determine the heat gradients on each side of the burning surface [3,9] this makes it possible to calculate the value of Q_s.

2.2.2. *Combustion mechanism of extruded double-base propellants (EDB)*

2.2.2.1. *The various zones of combustion*

Several combustion zones are observed (Fig. 2):

Zone 1 This is the zone where the propellant is not affected by the combustion, although its initial temperature T_i rises until it reaches the value beyond which the reactions in condensed phase are activated.

Zone 2 The foam zone, because of its foamy aspect. This is the zone where the decomposition processes of the solid phase occur in a very thin layer (10^{-2} to 10^{-3} cm) at moderately high temperature (600 K). Some endothermic transformations produce liquids and gases: they result from the thermal decomposition of nitrocellulose and nitroglycerine. Other reactions, on the other hand, are exothermic (reactions between decomposition products of the various propellant ingredients).

Zone 3 The fizz zone, because of the fizzing aspect of the combustion. This is the zone where the primary flame lies, resulting from the reactions between the nitrogen peroxide and aldehydes produced by the decomposition of the propellant. The proportions of the gaseous products depend on the propellant composition, and especially when there are specific ingredients controlling burning rate, called ballistic modifiers or burning rate catalysts. In this zone the temperature gradient is high; the adiabatic temperature of the primary flame is about 1300 K.

Zone 4 The dark zone, because of its color. In this zone the gaseous products produced by the primary flame are mixing; they become hotter because of the heat flux transmitted by zone 5.

Zone 5 The final flame zone. In this zone combustion is largely completed. The gaseous products produced by the primary flame have reached the concentration and temperature necessary for the chemical

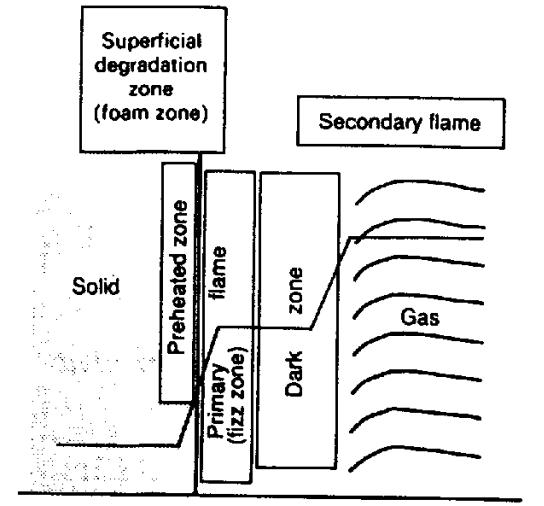

Surface		End of primary flame		End of secondary flame	
No_2	0.33	NO_2	---	NO_2	---
Aldeh.	0.35	Aldeh.	---	Aldeh.	--
NO	0.08	NO	0.25	NO	---
N_2	---	N_2	0.02	N_2	0.15
CO	0.1	CO	0.42	CO	0.28
CO_2	0.07	CO_2	0.15	CO_2	0.38
H_2O	0.03	H_2O	0.14	H_2O	0.19
H_2	0.001	H_2	0.006	H_2	0.004
		Hydroc.	0.03		

Mass decomposition ratio of the products in the different flame regions

FIG. 4.2. Burning zones of double-base propellants.

reactions to occur (NO/CO, H_2 reactions). The adiabatic temperature of the flame is around 2600 K.

2.2.2.2. *Burning rate law and formulation parameters*

The burning rate versus pressure law, for these propellants, depends on:

- the flame system;
- the apparition of a carbon deposit on the propellant burning surface.

The first part of this section presents the main trends for reference propellants (without ballistic modifiers). Because they are not interesting for practical use (very high pressure exponents), a second part discusses the behavior of propellants containing ballistics additives.

(a) Effect of pressure

At a specified pressure the intrinsic burning rate of an EDB propellant depends most of all on its composition (Chapter 9). There are:

- so-called "cold" propellants with a heat of explosion around 800 cal/g;
- "hot" propellants, more energetic (approximately 1300 cal/g) and having greater burning rates.

The distance of the flames from the surface is influenced by the pressure:

- Up to approximately 10 MPa, combustion is governed by the primary flame. The NO_2/aldehyde reaction has an activation energy of approximately 5 kcal/mole, and is distributed over the entire thickness of the fizz zone; in addition, its order of reaction, close to 1, should lead to an n value close to 0.5. The measured temperature of the flame, however, depends on the pressure [11], and is higher than the adiabatic temperature calculated for the NO_2/aldehyde reactions alone. Lengellé *et al.* [4] suggest that additional reactions between nitrogen monoxide and the surface carbon deposit be taken into account. This increase in primary flame temperature as a function of pressure level explains the high values of pressure exponents (around 0.75) that are observed with uncatalyzed propellants. 100bar
- At pressures above 10 MPa, the final combustion flame approaches the burning surface and, because of its tendency to merge with the primary flame, its heat flux also participates to the propellant decomposition. Because of its energy characteristics (order of reaction of 2), the pressure exponent is closer to one in this range of pressure.

(b) Effect of the ballistics modifiers

The introduction during manufacture of ballistic catalysts in the propellant compositions allows the regulation of the burning rate level and a significant decrease in the values of the temperature coefficient and of the pressure exponent. In the pressure range of rocket motors, exponent values close to zero can thus be obtained, thereby "flattening" the burning-pressure curve. The most common additives are:

- lead salts;
- copper salts, mixed with lead salts (copper components alone are not very active).

Their effect, depending on their amount, spreads over a certain range of pressures. They produce an increase in the burning rate of the propellant without catalysts (super-rate) while at the same time allowing the plateau effect. Addition of carbon black permits the displacement of the pressure range where the super-rate occurs.

(c) Initial super-rate

This occurs primarily at low pressure (<15 MPa). Experimental data published by Lengellé and Kubota show that the temperature of the primary flame is increased by the addition of burning rate modifiers. These appear to strengthen the reactions with the carbon deposited on the surface; in this case the deposits become thicker. It seems necessary, however, to invoke other mechanisms to explain the very strong effects observed: in some cases the thick carbon deposit seems to act as a flame-holder, bringing the final flame significantly closer to the surface.

(d) Second super-rate

This appears at high pressure. The carbon deposit on the surface has been eliminated. On the other hand, spots, probably lead monoxide, have been observed at the surface after extinction of strand burner samples.

Little is still known about the mechanisms that cause these super-rates, particularly at high pressure.

2.2.2.3. *The models*

It would not be feasible here to provide a detailed analysis of each model. We limit ourselves to citing the major ones:

- models taking into account, in various manners, the primary flame: Kubota *et al.* [11], Beckstead [12], King [13], and Cohen [14];
- simulations of the complete flame system: Ferreira *et al.* [15].

2.2.3. *Combustion mechanisms of heterogeneous propellants (inert and active binder propellants)*

Heterogeneous propellants contain a mixture of ingredients; each of them, when decomposing, releases gaseous products whose nature is either oxidizing or reducing. The initial mixture allows a complete combustion, based on the availability of chemical equilibria (Chapter 3). Nitramine molecules and energetic binders both contain combustible and oxidizing agents, ensuring a complete and independent combustion. In the following section we first briefly describe the behavior of each main ingredient when subjected to a significant heat source. This leads to a better understanding of the mechanisms observed in propellants.

2.2.3.1. *Decomposition of the main ingredients of heterogeneous propellants*

(a) Ammonium perchlorate (AP)

Differential scanning calorimetry [16] has shown:

- that solid AP experiences a change of phase that corresponds to a change in the crystal network at 513 K;
- the existence of two exothermic decomposition reactions in the condensed phase at approximately 570 K and 700 K.

Its melting point is 833 K. Linear pyrolysis tests have been performed by Coates and Guinet [10]. Results obtained by Seleznev *et al.* [17], however, who used an optical method to determine the burning surface temperature of strands, also serve as a reference.

AP combustion is sustained by the heat produced by the reactions in the condensed phase and the premixed flame which lies very close to the surface. The reaction between ammonia and perchloric acid, produced by AP decomposition (adiabatic flame temperature is 1205 K, order of reaction 2 and activation energy approximately 15 kcal/mole, as established by Guirao and Williams [18]), occurs at the surface. This reaction provides oxidizing species.

The pressure exponent is high (around 0.77 between 2 and 10 MPa) and there is a pressure threshold below which the combustion is no longer sustained. It corresponds to a surface temperature equal to the melting temperature of this oxidizer.

(b) Cyclic nitramines RDX and HMX

Two cyclic nitramines are used in propellant chemistry. The melting of these ingredients (approximately 477 K for RDX and 553 K for HMX) is a complex phenomenon: it has been observed, for instance, that the large particles liquefy easier than the small ones. Solid HMX comes in four different polymorphic forms, of which form β is the most common. The other forms (α, γ, δ) are successively obtained during a slow temperature rise. It is not known whether they exist under the rapid heating conditions occurring during combustion.

Boggs [19] and Fifer [20] have both written an exhaustive description of the results of decomposition studies of these nitramines. The decomposition reactions in the condensed phase lead to the rupture of the C-N and N-NO_2 chemical bonds. Analysis of pyrolysis gases shows the presence of N_2, N_2O, NO, CO_2, CO, H_2, HCHO, H_2O, and HCN. According to Fifer, the reaction controlling the combustion is the reaction between aldehyde and NO_2, very

rapid at the temperature reached. The flame temperature, contrary to the AP flame, is very high (3286 K for RDX and 3278 K for HMX).

The burning rate law for HMX was determined using monopropellant crystals or pressed strands [21]. Sample observation after extinction shows the presence of a melted layer on the surface during combustion, with a thickness depending on the pressure.

(c) The binder

In this section we only describe the case of inert binders, because the combustion mechanisms of energetic binders are identical to homogeneous propellant ones.

An inert binder is a polymer where C-C or C-H chemical bonds prevail. Under the effect of heat these bonds break down. This reaction may occur in the solid or the liquid phase, depending on the nature of the polymer. This heat-related degradation results in the appearance of hydrocarbons that are:

- polymerized at the surface in the form of a charcoal residue or "char", in some cases;
- gaseous, and, when placed in an oxidizing atmosphere, burn with diffusion flames.

The binder pyrolysis law can also be evaluated by thermogravimetry.

(d) Aluminum

Its introduction in compositions containing ammonium perchlorate allows a significant increase of their adiabatic combustion temperatures. This effect is due to the additional reaction for the formation of metal oxide. Since the melting temperature of aluminum is 933 K, the micron-size particles contained in the propellant melt at the surface where the temperature is generally higher, and they gather into aluminum droplets. A detailed description of the combustion of aluminum has been done [10]. In order to facilitate the comprehension of the models, we shall only state that:

- the liquid droplets leave the surface and are oxidized at a significant distance from the surface;
- the alumina particles formed in the combustion chamber of the propellant grain are very small (approximately a few microns) and liquid (Al_2O_3 melts at 2318 K); they agglomerate or burst before they solidify inside the nozzle, which ensures the gas expansion;
- Aluminum combustion is usually fairly well completed inside the chamber. Some configurations, however, may decrease its efficiency when aluminum residence time in the combustion chamber is too short.

2.2.3.2. *Combustion mechanisms of inert binder propellants*

The following solid particles are dispersed in the binder matrix:

- oxidizer particles with large particle size distribution (1–400 μm);
- and possibly, aluminum particles.

The following occurs during combustion:

- In the gaseous phase: all of the combustion reactions resulting in the appearance of a complex flame system (Fig. 3):
  reactions involving AP;
- In the gaseous phase: all of the combustion reactions resulting in the appearance of a complex flame system (Fig. 3):
  - premixed AP flamelets, considered as monopropellant. AP adiabatic temperature, at a realistic operation pressure in the range of 7 MPa, is approximately 1230 K;
  - diffusion flames between the oxidizing products resulting from AP decomposition or from AP premixed flame and the hydrocarbons produced by the binder; the adiabatic temperature of the final diffusion flame, for a non-metallized propellant containing 80% AP, is in the range of 2300 K.

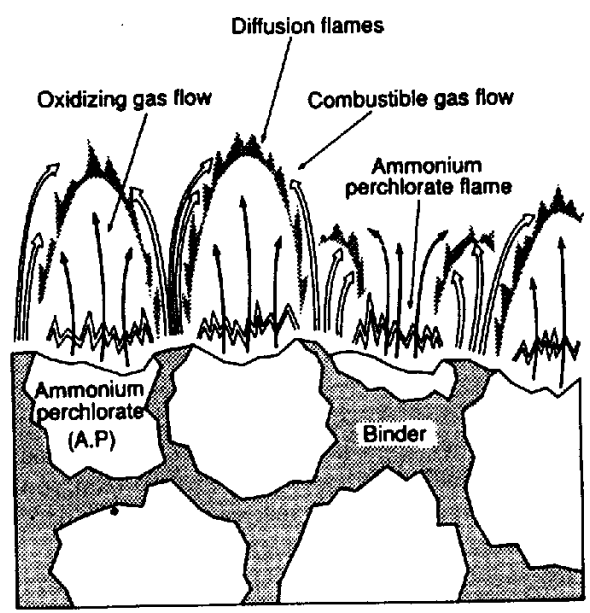

FIG. 4.3. Flame structure of heterogeneous propellant with inert binder.

(a) Burning rate law and composition parameters

For these propellants the burning rate law is a function of:

- the pressure range;
- the AP size distribution.
  - — At very low pressure, the burning rate is low and the heated thickness of propellant is large compared to the size of AP particles. Because the gaseous reactants produced by the various ingredients have had time to mix, combustion is controlled by chemical kinetics. The influence of the AP particle size is weak and the pressure exponent is high.
  - — At medium pressure (1–15 MPa), the thickness of heated propellant is less than above, and the diffusion phenomena between the reactive gaseous products become controlling phenomena. Premixed and diffusion flames are simultaneously observed, and the pressure exponent value is moderate (0.3–0.4). In this pressure range the burning rate is closely tied to the AP particle size: the finer the ammonium perchlorate, the greater the burning rate.
  - — At very high pressure ($p \geq 15$ MPa), a new regime appears, with a higher pressure exponent (0.6–0.7). The current models do not predict this. It could be explained by a modification of the AP pyrolysis law at high pressure. We may also think that under the effect of the increase of velocity of the exhaust gases coming out of the surface, or caused by the high pressure level, the heat transfers are increased, in turn increasing the flux transmitted to the propellant.

(b) Influence of ballistics additives

The additives used contain metallic atoms. Their action results less from chemical reactions than from modifications of the thermal properties of the burning surface:

- Some additives cause the formation of a very thin residue on the surface. They must be well dispersed inside the propellant to ensure the most efficient effect. Liquid additives are, for this reason, vastly preferable (particularly for small oxidizer particle sizes), which explains the good results obtained with ferrocenic additives.
- Other additives induce an increase of heat transfers as the diffusion flame stands closer to the burning surface. In this particular case, metallic oxides with sufficiently large particle size are used as flame-holder.

(c) The models

From the various existing models [22], we would like to point out that:

- The first model developed by Summerfield *et al.*, the GDF model (granular diffusion flame), studies the combustion reaction of oxidizing gaseous "pockets" in the gaseous flow of binder decomposition gases. Assuming that the size of these pockets is equal to the size of the solid AP particles, there are two burning regimes:
  - — a low-pressure, premixed flame regime,
  - — a high-pressure, diffusion flame regime.

The resulting law is usually verifiable, up to approximately 15 MPa:

$$\frac{1}{r} = \underbrace{\frac{a}{p}}_{\text{premixed regime}} + \underbrace{\frac{b}{p^{1/3}}}_{\text{diffusion regime}}$$

where a and b (linked to AP particle size) are constant.

- Hermance calculates the mass flow rates of the binder and of the oxidizer, and introduces the notion of delayed ignition of the AP particles as well as a binder/oxidizer reaction at the surface. He takes into account the possibility of a "turbulent regime" caused by the heterogeneity of the combustion at the propellant surface. This regime modifies the thermal characteristics of the gases and causes an increase of the pressure exponent when the flow rate is significant.
- The BDP Model (Beckstead *et al.* [8]) takes into account a complex and more realistic flame system: a control parameter is used to adjust the flame's relative importance in accordance with the pressure range. At low pressure the primary flame is prevalent ($HClO_4$/hydrocarbon). At high pressure it is replaced by the AP premixed flame and the final diffusion flame (oxidizing products produced by the AP/hydrocarbon flame). Binder and AP surface temperatures are assumed to be the same. A statistical analysis using pyrolysis laws and taking into account the AP size distribution, reputed to be unique, allows calculation of the binder and AP mass flow rates.
- The PEM model (Petite Ensemble Model) offers the possibility of performing a more detailed analysis of the heterogeneities of the surface, coming from a better modeling of oxidizer particle size distribution. By supposing that each flamelet is linked to a particle surrounded by a thin binder coating, and that all these small flames do not interact among themselves, the propellant can be regarded as a collection of simpler propellants (one particle size log-normal distribution) called pseudo-propellants. The description of the combustion of each pseudo-propellant uses the same flame system as the BDP model. Its mass flow rate is calculated on the basis of AP particle combustion as a function of time.

As in the case of BDP, mathematical formulae allow for evaluating geometry of the pseudo-propellant burning area. The PEM model assigns an identical value to the surface temperature for the binder and the oxidizer of each pseudo-propellant. The burning rate of the entire propellant is determined by averaging the burning rates of each pseudo-propellant.

- In France, the method developed by ONERA [23] is similar to the last two models. The flame system is the BDP system, with the exclusion of the primary flame. The calculation of the mass flow rate is also done as a function of the combustion time of a particle. But the pyrolysis of the ingredients is determined by using two different surface temperature values, one for AP and the other for the binder. Like the PEM model this method allows computations for several different values of the filler particle size.

2.2.3.3. *Combustion mechanisms of advanced energetic binder propellants*

RDX or HMX, which significantly increase the specific impulse, are introduced in the EDB-type binder. These are the so-called composite modified double-base propellants. They are divided into two families (CMCDB and XLDB), based on their manufacturing process and resulting different ballistics characteristics (Chapter 11). Because their combustion mechanisms are very similar, the following section discusses only those related to XLDB propellants. Their performance level may be further increased by adding ammonium perchlorate and aluminum to their ingredients (NEPE propellants). The preceding discussion on the various ingredients behavior of homogeneous and heterogeneous propellants will now help to understand better the combustion mechanisms of these two major families of solid propellants.

(a) Combustion mechanisms of XLDB propellants

Observation of the burning area

By observing the combustion of samples, we see that nitramine particles melt at the surface, under the effect of heat flux. Therefore an intimate mixture, close to the surface, of the various gaseous species takes place, facilitating reactions led by premixed flames. We know that the nitramine molecule has a balanced amount of oxidizer and reducer. In addition, the combustion products are mostly N_2, CO, and H_2O. Since the products of the primary flame are mainly NO, CO, and H_2, we may safely assume that there is no interaction between the various flame systems.

Burning rate law and formulation parameters

The burning rate law of a polyester binder is shown in Fig. 4. It is close to that of a "cold" extruded double-base propellant. We also see, in this figure,

that it is slightly modified by the addition of nitramine. The propellant burning rate realizes a compromise between the burning rate of the binder and that of the nitramine. Experience has also shown that the size of the particles has no effect on burning rate: this is explained, at least at low pressure, by the nitramine melt layer at the surface. Finally, we see that the exponent remains very high, regardless of the pressure level.

Influence of the ballistic catalysts

Fifer [20] has summarized the main results already known concerning the catalysis of these propellants. When researching ballistic catalysts it is necessary to act either on binder or on nitramine.

- Catalysts of binder decomposition

  Catalysts used with homogeneous propellants (lead salts) develop a carbonized layer at the surface, leading to a strengthening of the NO-C reactions. They cannot, however, all be used with a polyester binder, because they catalyze the cross-linking reaction, resulting in an unacceptable rise of propellant viscosity during processing. Some of these catalysts induce super-rates, although less spectacular than with homogeneous propellants: the thickness of the carbon deposit at the surface is, in this case, certainly less than with nitroglycerine- and nitrocellulose-based propellants.

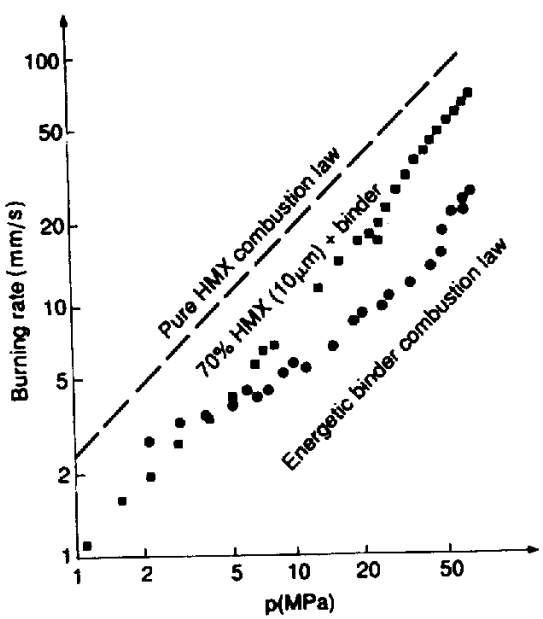

FIG. 4.4. Burning rate laws for propellant and basic ingredients.

- Additives facilitating nitramine decomposition

  Because of the large quantities of nitramines added to the propellant, another possibility consists in facilitating the decomposition of the filler. Today, part of the research efforts are oriented to the development of products that would have such effects.

(b) Combustion mechanism of NEPE propellants

Observation of the burning area

Current compositions use a polyether binder, more heavily oxygenized than a polyester binder. In addition to the nitrated plastifier and the nitramines already contained in the XLDB propellants, NEPE propellant performance is increased by adding ammonium perchlorate and aluminum.

By introducing ammonium perchlorate, the structure of the flame zone is significantly modified. Oxidizing species resulting from AP decomposition and hydrocarbons produced by the binder form diffusion flames leading to the disappearance of the very characteristic dark zone. The flame of a NEPE propellant is very much like the flame of a heterogeneous inert binder propellant.

Burning rate law and composition parameters

- Behavior of the binder

  Although the burning rate laws of polyether and polyester binders are very close, when ammonium perchlorate is added the polyether binders show very peculiar behavior. Experience has shown that it is capable of dissolving a non-negligible quantity of AP; saturation was seen at a 6% mass ratio value of AP/(AP + binder). The portion of dissolved AP brings about the appearance of a premixed flame with the gaseous products of the binder. The burning rate of the so- "filled" binder increases rapidly and its pressure exponent is high.

- Propellant burning rate law

  Due to the formation of diffusion flames, the propellant burning rate depends on the AP particle size. While keeping constant AP content in a formulation, the burning rate can be improved by using micron-size particles. The addition of increasing quantities of AP promotes the formation of diffusion flames, particularly in the cases of medium or large particle sizes; lowering of pressure exponent is subsequently observed.

3. Steady-State Combustion in a Solid Propellant Rocket Motor

The causes of the modification of propellant burning rate law are studied in this section which also deals with methods used to predict the steady-state operation of a rocket motor.

3.1. MODIFICATIONS OF THE BURNING RATE LAW INDEPENDENT OF THE INTERNAL AERODYNAMIC FIELD

3.1.1. Modifications caused by involved materials

3.1.1.1. Modifications occurring at the propellant/insulator interface

In the case of an end-burning combustion mode, the solid propellant grain is particularly susceptible to this phenomenon. An analysis of the burning front after quenching often shows a surface deformation, easily explained by a modification of the burning rate in the immediate vicinity of the thermal insulator (Fig. 5).

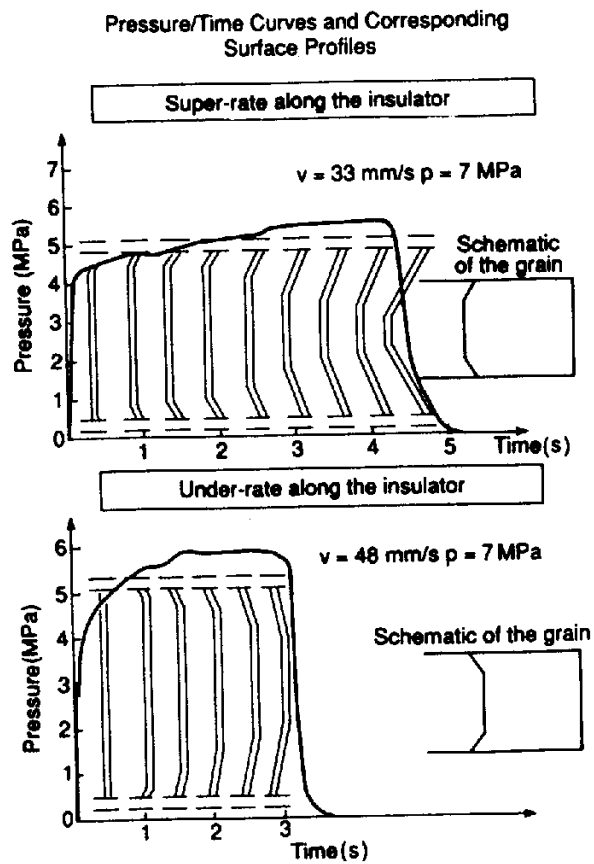

FIG. 4.5. Visualization of the regression front of an end-burning grain.

(a) Origin of local burning rate modification

- Large concentration of fine particles in the area close to the inhibitor, or peculiar distribution of the particles in that area

  These particles may be ammonium perchlorate, anti-instability additives, or ballistics catalysts used in solid form. If finely divided, all these ingredients increase the burning rate values. Messner [24] indicates that super-rate values of 70% have been obtained with compositions containing iron oxide. Smith [25] comments on tests demonstrating the accumulation of AP close to an interface. Jolley *et al.* [26], however, believe that this behavior does not systematically occur.
- Migration of propellant liquid ingredients at the interface

  During curing, when the propellant is still a dough, and to a lesser degree during aging, the migration of the plasticizer and/or of the ballistic additive may occur. Any displacement of the plasticizer in the inhibitor leads to a local increase in the propellant filler content as well as to a growth in the burning rate. Conversely, a local thinning in ballistic additives content of the propellant decreases the burning rate, but the progression of the flame front in parallel layers tends to counteract this effect.
- Conduction heating of the material near the interface

  This phenomenon, resulting from the heat transfer to the motor walls caused by gas flow inside the combustion chamber, occurs consecutively to the temperature rise of the propellant in immediate contact with the heated materials. This situation is more likely to happen during the firing of solid free-standing end-burning grains. The flow of heated gases in the gap between the case and the grain may induce local heating of the insulator and of the propellant in contact.

(b) Remedial measures

- In the case of active binder propellant grains

  Here we are concerned with the absorption of nitroglycerine by the thermal insulator: the propellant heat of explosion locally decreases, but the percentage of ballistic additives is clearly increased. The use of highly cross-linked inhibitors or silicones is recommended. A primer (polyisocyanate) may also be interposed, which, delaying ingredients migration, provides the insulator with sufficient time to acquire mechanical strength. When thermal heating of materials occurs near an interface, the addition of an ingredient with endothermic decomposition may prove useful to limit the super-rate.
- In the case of inert binder heterogeneous propellant grains

  The super-rate decreases by slowing down migration of the plasticizer in the bonding resin, usually of a polyurethane type. This can be done by using high cross-linked polyurethanes or primers acting as barriers against migrating species.

3.1.1.2. Controlling the burning rate

(a) Technology used

There have been a large number of studies to evaluate the advantage of end-burning propellant grains with locally controlled burning rates. Two techniques were examined.

- The first technique consists in incorporating strands of propellant perpendicular to the surface, these strands having a higher burning rate than the matrix propellant. No heat exchange occurs between the two propellants because they are good heat insulators, and the angle of resulting cones in the slower composition depends on the ratio between burning rates at the specified operating pressure [27];
- With the other technology, the super-rate effect is obtained by incorporating metal wires inside the propellant grain. These wires melt at a relatively low temperature, conduct the heat very well, and transmit a heat flux to the adjacent propellant, raising its initial temperature and therefore its local burning rate. The wires used are typically made of copper or silver. The design of these wired grains is discussed in Chapter 2.

3.1.2. The hump effect

3.1.2.1. The phenomenon

The hump effect — also called BARF, BRAF, SBRE or RAINBOW when used to indicate the effects due to mechanical stresses in composite propellant grains — refers to an overpressure during firing that may reach 8% of the planned value. This overpressure is not constant during operation. The corresponding time depends on the propellant grain geometry. In a BATES grain, for instance, it corresponds to the point where approximately half the web is burned. This phenomenon may occur in many internal configurations: it has also been observed on star-shaped grains.

The result analysis of such a firing is based on internal ballistics laws, assuming that the burning rate law of the propellant is the same in any point

of the grain. This analysis then provides the evolution of the burning area, becoming an equivalent area, as a function of the burnt thickness. When the hump effect occurs during a firing, comparison of the previous analysis with the theoretical curve of the evolution of the burning area clearly demonstrates the presence of differences (Fig. 6). Those primarily depend on AP, its ratio and size distribution in coarse and fine particles [27,28], and on the presence of aluminum in the composition.

3.1.2.2. *Influence of processing*

An analysis of results obtained after extinction of a BATES propellant grain at the maximum value of overpressure, shows that hump effect is caused by a burning rate law change as a function of the propellant thickness. Friedlander and Jordan [28] offer the same interpretation. The explanation may be a peculiar distribution of the propellant solid fillers, induced by the manufacturing process.

3.1.2.3. *Taking the hump effect into consideration for ballistics predictions*

Currently, it is only through accumulating results analyses from firings that an average and empirical law of burning rate deviations for a specific propellant grain may be obtained, of the form:

$$\frac{r_r}{r_0} = f(e)$$

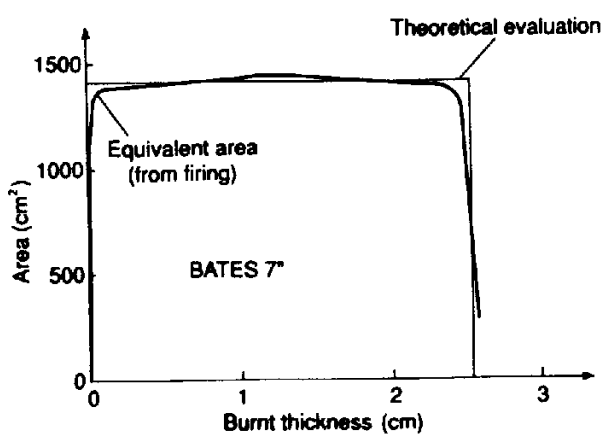

FIG. 4.6. Comparison of burning area evolutions of a BATES grain.

where:

r_r is the actual burning rate of the propellant during firing;
r_0 is the known burning rate of the propellant, excluding the hump effect;
e is the burnt thickness.

As a rule, the ratio r_r/r_0 varies by 5% in a range from 0.95 to 1.05. For some grain shapes (tubular, star) with a mainly radial burning the above law exhibits a hump when plotted. For more complex shapes (FINOCYL type) with a combination of several types of combustion (in R, Z and θ), the curve has the shape of a sinusoid.

Currently, precise ballistics predictions presuppose a sufficient number of results from experiments the analysis of which helps estimating the $r_r/r_0 = f(e)$ law which has to be considered in the computations.

3.1.3. *Mechanical stresses*

Mechanical stresses occur in case-bonded propellant grains:

- during the cooling period after propellant curing;
- during operation, when the combustion chamber is pressurized.

In some cases these stresses modify the burning rate law.

3.1.3.1. *At the bonding interface*

Kallmeyer *et al.* [30] demonstrate the increase of the super-rate at the propellant/inhibitor interface as a function of the bonding stress level; this stress level is a function of the difference between curing and firing temperatures.

3.1.3.2. *Inside the propellant*

Internal stresses cause dewetting to occur between the various fillers and the binder; dewetting increases with load intensity. As a result the propellant acquires a certain internal porosity and becomes compressible. An increase in the burning rate is then observed [31]. Figure 7 illustrates this effect on a strand which has been first strained, then inhibited with a stiff agent strong enough to maintain elongation. The burning rate change does correspond to the beginning of the strand volume variation.

3.1.4. *Acceleration*

The motor operation, in flight, may be modified by the acceleration of the rocket. This modification is particularly clear with aluminized propellant grains.

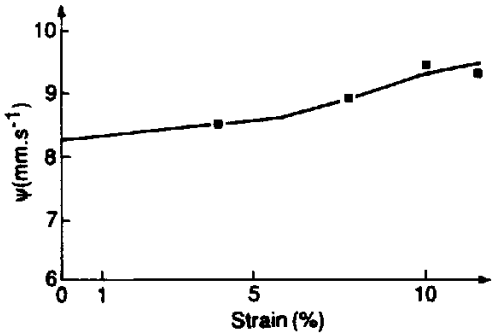

FIG. 4.7. Influence of propellant elongation on the burning rate law. Burning rate vector parallel to the tensile stress.

Extinguishments have shown that the burning surface of this type of propellant, when submitted to a normal acceleration directed toward the propellant, exhibits a large number of small conical craters. They are caused by amounts of aluminum droplets which contribute to heat conduction at the surface and consequently significantly increase the burning rate at the point of contact. When an aluminum droplet becomes larger (and probably oxidizes), the burning rate at the bottom of the crater slows down (though remaining greater than the burning rate without acceleration). The bottoms of the craters flatten themselves out.

Based on studies done on this subject, and illustrated by Fig. 8, we note that this type of phenomenon occurs when:

- the acceleration exceeds a threshold value which is a function of the size of the aluminum particles and of the burning rate (approximately 10 g for

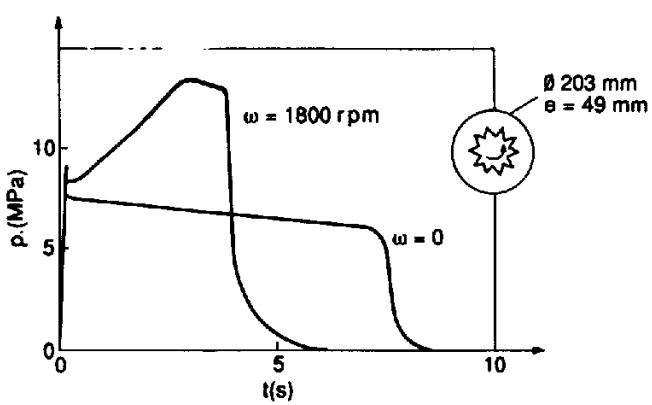

FIG. 4.8. Effect of acceleration on motor operation.

propellant grain burning at 5 mm/s and containing aluminum particles measuring 5 μm);
- the angle between the acceleration and the burning surface normally does not exceed a threshold value (of about 20°); beyond that value, the influence of acceleration on the burning rate is negligible.

3.2. DETERMINATION OF THE FLOW FIELD

3.2.1. Background and fundamentals

The simplified analysis [33] of the motor stationary operation is based on the possibility of realizing equilibrium between:

- the mass flow rate produced by the burning surface of the propellant grain;
- the mass flow rate the nozzle can eject.

The steady-state regime resulting when the two are matched, and related specific fundamental equations, were discussed in Chapter 1. Continuing to assume that combustion and expansion of burned gases form two separate phenomena, respectively taking place in the combustion chamber and in the nozzle, we are able to analyze the transient regime associated with grain ignition and burn-out phases.

3.2.1.1. *Transient regime*

While we disregard the volume variation of the central port resulting from combustion (rather small since transient phases are short), we do include the term representing internal gaseous mass variations, which stands for the filling (or emptying) of the central port, and is tied to gas compressibility. Therefore the exhaust mass flow rate coming out of the nozzle corresponds to the mass flow rate emitted by the propellant burning surface less the build-up term. The continuity equation is written:

$$t_s \frac{dp_c}{dt} + p_c = \frac{\dot{m}}{C_D A_t} \tag{11}$$

where:

$t_s = V/(r\, T_c\, C_D\, A_t)$ = the residence time;
V = volume of the chamber;
p_c, T_c = pressure and temperature of the chamber;

A_t = area of the nozzle throat;
$\dot{m}$ = mass flow rate of the propellant grain;
C_D = propellant discharge coefficient;
r = R/M where R is the ideal gas constant, M is the gas molecular weight.

(a) Pressurization

Assuming the validity, under these conditions, of the steady-state burning rate law as well as instantaneous ignition of the entire surface of the propellant grain, the pressure evolution is given by:

$$p_c = p_{c0}\left\{1 - \exp\left[1 - (1 - n)\frac{t}{t_s}\right]\right\}^{1/1-n} \quad (12)$$

where p_{c0} is the chamber pressure corresponding to stationary operation.

(b) Depressurization

Assuming a sudden extinction of the entire surface, we have:

$$p_c = p_{c0} \exp\left(-\frac{t}{t_s}\right) \quad (13)$$

3.2.1.2. *Requirements when designing a propellant grain*

The steady-state regime assumption of Chapter 1 and the simplified reasoning above turn out to be insufficient, for several reasons:

- It only gives an average value for the pressure. This pressure level is uniform in the entire combustion chamber. Its evolution, as a function of propellant thickness, is known as long as the operating point can reasonably be approximated by a succession of discrete equilibria.
- The pressure variations inside the combustion chamber are not determined; they must be known to assess the structural integrity of the propellant grain, particularly at the onset of the firing. They also must be determined in conjunction with the local burning rate expressions (e.g. eqn (1)).
- The gas velocity inside the combustion chamber being assumed to be zero, risks connected with heat transfer increase, as well as erosive burning, cannot be taken into consideration.

- There is no modeling of the non-steady phenomena: eqns (12) and (13) hold a limited validity for the transient sequences. In addition these assumptions do not include variations of the propellant discharge coefficient.

More complete models should include unsteady phenomena and are therefore necessary for a precise knowledge of the internal aerodynamics.

3.2.2. *Conservation equations in fluid mechanics*

The fluid domain consists of the combustion chamber and nozzle. Some of the boundaries are inert ones, i.e. inert parts of the combustion chamber and of the nozzle. The burning surface, on the other hand, is an injecting boundary which, over time, moves along its normal at a velocity r (propellant burning rate law).

SNPE computer codes solve the fluid mechanics equations while respecting the conservation conditions relative to the mass, momentum and energy, within a framework of restrictive assumptions concerning the nature of the fluid and its heat exchanges with the case walls:

- The fluid produced by the propellant combustion is a gas assumed to be ideal and heated at a high temperature.
- The fluid is non-viscous, non-reacting and non-conductive. There is no heat exchange with the walls. The boundary with the burning propellant occurs at the end of the flame; the flame height is assumed to be negligible.
- The fluid is single-phased. There is no need to introduce the condensed phase because neither the pressure fields nor the burning rate are basically modified by its presence. It should, however, be taken into consideration in any realistic performance prediction (Chapter 3).

3.2.3. *Solving the one-dimensional equations*

3.2.3.1. *Local equations*

Each term of the conservation equations will be assessed in the fluid sector shown in Fig. 9. This sector has two stationary boundaries (A_1 and A_2) and a moving boundary S.

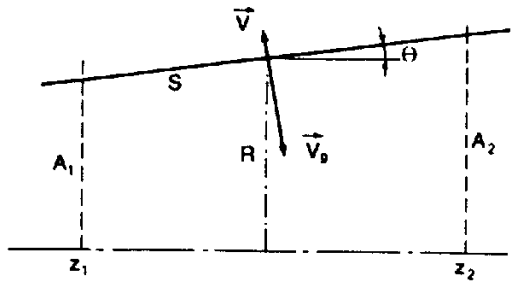

FIG. 4.9. Element of fluid. One-dimensional assumption.

(a) Absolute velocity of the gases at the combustion wall

The fluid velocity at the wall is assumed to be the exhaust gas velocity released at the wall. Here, the equation of mass conservation requires:

$$\rho \vec{v}_r = \rho_p \vec{v} \tag{14}$$

where:

ρ, ρ_p = density of, respectively, the gases and the propellant;
$\vec{v}_r$ = velocity of the gases relative to the wall;
$\vec{v}$ = absolute velocity of the wall.

Therefore:

$$\vec{v}_r = \vec{v}_g - \vec{v} \tag{15}$$

where $\vec{v}_g$ is the absolute velocity of the gases at the wall.

Taking into account the respective orientation of each of the vectors, we find:

$$v_g = v\left(\frac{\rho_p}{\rho} - 1\right) \tag{16}$$

(b) Continuity

With:

$\vec{u}$ = flow velocity vector
$\vec{n}$ = vector perpendicular to the surface. The term of the exhaust flow is calculated for A_1, A_2, and S (the normal directed outside the field)

from:

$$[\vec{u} - \vec{v}]\cdot\vec{n}\Big|_{A_1} = \vec{u}\cdot\vec{n} = -u(z_1) \tag{17}$$

$$[\vec{u} - \vec{v}]\cdot\vec{n}\Big|_{A_2} = \vec{u}\cdot\vec{n} = u(z_2) \tag{18}$$

$$[\vec{u} - \vec{v}]\cdot\vec{n}\Big|_{S} = \vec{v}_g\cdot\vec{n} - \vec{v}\cdot\vec{n} = -(v_g + v) \tag{19}$$

knowing that:

$$dS = 2\pi R\frac{dz}{\cos\theta};\quad \frac{\partial A}{\partial t} = 2\pi R\frac{v}{\cos\theta}$$

and for a small dz increase, we have:

$$\frac{\partial}{\partial t}(\rho A) + \frac{\partial}{\partial z}(\rho u A) = \rho_p\frac{\partial A}{\partial t} \tag{20}$$

(c) Momentum

Assuming a uniaxial flow along the z axis, the projection on z of the tensorial product of the equation below must be calculated:

$$\frac{\partial}{\partial t}\int_{V(t)}\rho\vec{u}\,dV = -\int_{S(t)}\rho[\vec{u}\otimes(\vec{u}-\vec{v})]\vec{n}\,dS - \int_{S(t)}(pI + T)\vec{n}\,dS$$

where:

T = deviator of the tensor of the second order, representative of viscous tensions;
I = identity matrix;
$V(t)$ = moving volume limited by the surface $S(t)$

We obtain:

$$\text{Proj on } z[\vec{u}\otimes(\vec{u}-\vec{v})]\vec{n}\Big|_{A_1} = [\vec{u}\otimes\vec{u}]\vec{n}\Big|_{A_1} = -u^2(z_1) \tag{21}$$

$$\text{Proj on } z[\vec{u}\otimes(\vec{u}-\vec{v})]\vec{n}\Big|_{A_2} = [\vec{u}\otimes\vec{u}]\vec{n}\Big|_{A_2} = u^2(z_2) \tag{22}$$

$$\text{Proj on } z[\vec{u}\otimes(\vec{u}-\vec{v})]\vec{n}\Big|_{S} = -v_g(v_g + v)\sin\theta \tag{23}$$

Taking into account that $\partial A/\partial z = 2\pi R\ tg\ \theta$, and by making z_1 approach z_2, we obtain:

$$\frac{\partial}{\partial t}(\rho u A) + \frac{\partial}{\partial z}(\rho u^2 A) + A\frac{\partial p}{\partial z} = \rho_p v^2 \frac{v_g}{v}\frac{\partial A}{\partial z} \tag{24}$$

(d) Energy

When it is integrated over the volume $V(t)$, the local conservation equation for energy gives:

$$\frac{\partial}{\partial t}\int_{V(t)} \rho\left(e + \frac{\vec{u}^2}{2}\right)\mathrm{d}V = -\int_{S(t)} \rho\left(e + \frac{\vec{u}^2}{2}\right)(\vec{u} - \vec{v})\vec{n}\,\mathrm{d}S$$

$$-\int_{S(t)} (p\cdot\vec{u} + T\cdot\vec{u})\vec{n}\,\mathrm{d}S - \int_{S(t)} \vec{q}\cdot\vec{n}\,\mathrm{d}S$$

The various terms are assessed as above, and the local expression is written:

$$\frac{\partial}{\partial t}(\rho\varepsilon A) + \frac{\partial}{\partial z}(\rho\varepsilon u A) + \frac{\partial}{\partial z}(puA) = \frac{\partial A}{\partial t}\left[p\frac{v_g}{v} + \rho_p\cdot\varepsilon_b\right] \tag{25}$$

where:

ε = total internal energy of the gaseous discharge, $e = u^2/2$, where e represents the internal energy of the fluid;

ε_b = total internal energy of burned gases as they are created $= e_b + v_g^2/2$, where e_b represents the internal energy of the burned gases.

3.2.3.2. *Computer codes for calculations of one-dimensional equations*

There are several codes, because the one-dimensional assumption is fairly well justified for propellant grains with a high "length versus diameter" ratio and a gas flow section area that evolves slowly. This assumption allows rapid executing times. We will limit ourselves to one example: PROCNE 1 [34], which is very widely used for preliminary propellant grand design analyses.

The unsteady terms of the conservation equations are taken into account. The fluid domain is shared into discrete sections along the axis of the propellant grain: it includes the combustion chamber and the nozzle. The

numerical procedure selected for this code is the fractional two-steps method, proposed by Yanenko [35]. PROCNE 1 code is used to calculate the evolution of the internal aerodynamic field while taking into account the geometry evolution as a function of time. Figure 10 compares predicted pressure and thrust levels to experimental results for a nozzleless motor.

3.2.4. *Calculation of conservation equations for complex geometries*

Improved ballistics performances of rocket motors are obtained through propellant volumetric loading fraction enhancement, typically realized with complex geometrical shapes. Such configurations entail the presence of significant variations in the pressure and fluid velocity, as well as the possibility of couplings between the propellant burning rate law and the local

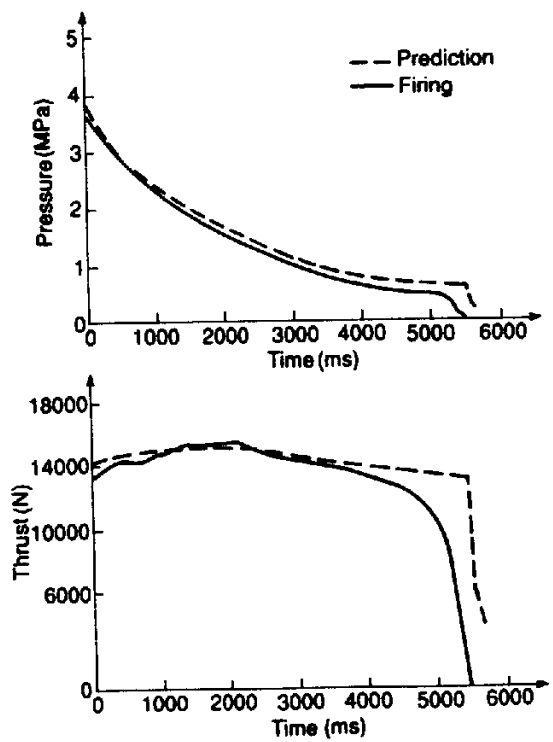

FIG. 4.10. Comparison between prediction (PROCNE) and experiment (nozzleless motor).

aerodynamic field. Consequently, the fluid mechanics equations must be resolved in a situation which is as representative as possible.

3.2.4.1. *Fundamentals of the two- and three-dimensional codes*

The numerical scheme used to solve the governing equations was created by Godunov *et al.* [36]. A few reminders on shock waves and discontinuity decomposition are necessary before discussing this procedure.

(a) Shock waves

First, some fluid mechanics notions: given a source S of small perturbations in a motionless fluid or in a uniform motion (Fig. 11):

- Motionless fluid: $u = 0$

A perturbation occurring at time $t = 0$ propagates at the speed of sound a in all directions and occupies at time t a spherical surface with a radius value of at.

- Fluid in uniform translation, with $u < a$

In a subsonic flow the perturbation spheres are inside each other, and surround the source. With sufficient time the perturbations reach every point of the fluid.

- Fluid in uniform translation, with $u > a$

In a supersonic flow the perturbation waves occur within an envelope. Only the areas within that envelope are affected by the perturbations.

- Formation of a discontinuity

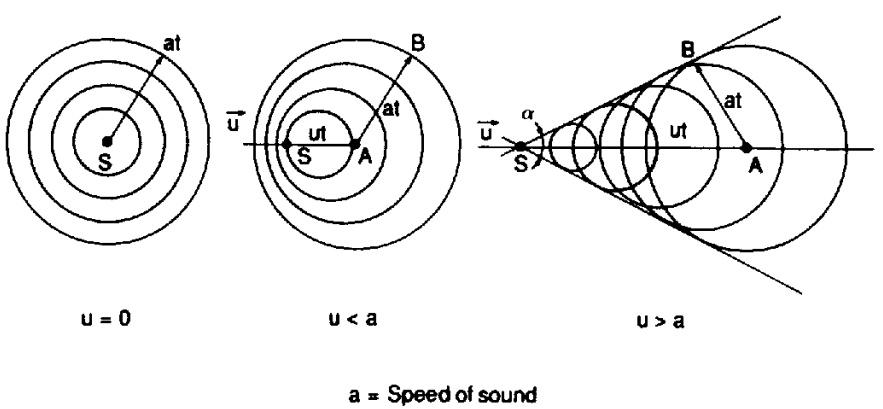

FIG. 4.11. Propagation of small perturbations in a uniform flow fluid.

In a fluid activated by a slight compression the successive waves will propagate faster and faster because of the rise in temperature of the medium, finally catching up to each other and forming a compression wave. In the opposite case, when the fluid is subjected to a slight expansion, the waves no longer catch up with each other because of temperature decay: a discontinuous expansion wave does not occur in most gases, although it may occur in some computational methods.

- Evolution through a flat discontinuity surface (Fig. 12)

When going through a discontinuity surface a compressible fluid is subjected to finite pressure and temperature variations, but its velocity suddenly varies in magnitude as well as in direction. The conservation equations on the ABCD volume are written as follows:

- Mass conservation

$$\rho_1 u_{1n} = \rho_2 u_{2n} \tag{26}$$

- Momentum conservation

$$p_1 + \rho_1 u_{1n}^2 = p_2 + \rho_2 u_{2n}^2 \tag{27}$$

where $u_{1t} = u_{2t}$

- Energy conservation assuming adiabaticity:

$$\frac{u_{1n}^2}{2} + \frac{\gamma}{\gamma - 1}\frac{p_1}{\rho_1} = \frac{u_{2n}^2}{2} + \frac{\gamma}{\gamma - 1}\frac{p_2}{\rho_2} = \frac{\gamma + 1}{2(\gamma - 1)}\left[c^2 - \frac{\gamma - 1}{\gamma + 1}u_{1t}^2\right] \tag{29}$$

where $c = \sqrt{\dfrac{2(\gamma - 1)}{\gamma + 1} c_p T_c}$

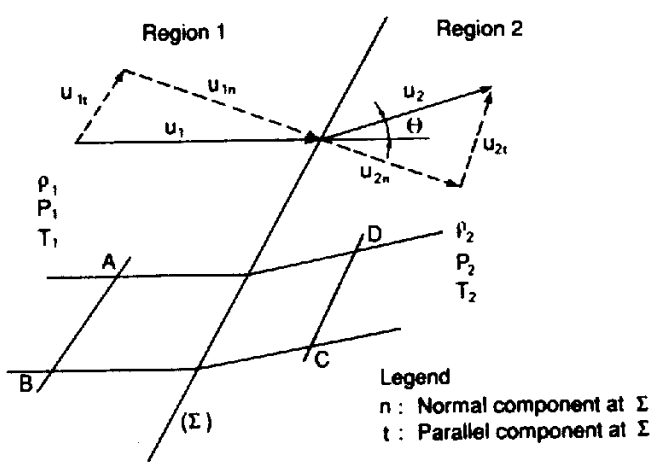

FIG. 4.12. Flow field evolution through a discontinuity surface (Σ).

to which the equation of the ideal gas state is added:

$$p_1 = \rho_1 r T_1; \quad p_2 = \rho_2 r T_2$$

where $r = R/M$ = specific gas constant

Hugoniot/relationship

This determines the relationship between p_1, ρ_1, p_2 and ρ_2

$$\frac{\rho_2}{\rho_1} = \frac{1 + \dfrac{\gamma + 1}{\gamma - 1}\dfrac{p_2}{p_1}}{\dfrac{\gamma + 1}{\gamma - 1} + \dfrac{p_2}{p_1}}$$

This relation is definitely different from the isentropic:

$$\left(\frac{\rho_2}{\rho_1}\right)^{\gamma} = \frac{p_2}{p_1}$$

Through a shock wave, the fluid therefore undergoes an irreversible evolution. The entropy for an ideal gas is given by:

$$s = c_v \ln\left(\frac{p}{\rho^{\gamma}}\right) + \text{constant}$$

The Hugoniot relationship expresses an actual physical evolution only when it corresponds to an increase of entropy.

(b) Process for discontinuities analysis

Godunov *et al.* [36] propose the following method: when two masses of the same gas, assumed ideal and compressed at different pressure levels, come into contact, the contact surface forms a discontinuity surface within the initial pressure distribution. The physical values on each side of the surface may undergo any sort of jump. Discontinuity, however, can exist as a stable formation only if it satisfies certain conditions; if not, it breaks down into several discontinuities becoming distant from each other with time. Consequently, several configurations may occur. Pressure and velocity values on each side of the contact discontinuity are identical; density and internal energy differ, on the other hand. These two fields are themselves separated from the non-perturbed area by either a shock wave or an expansion wave.

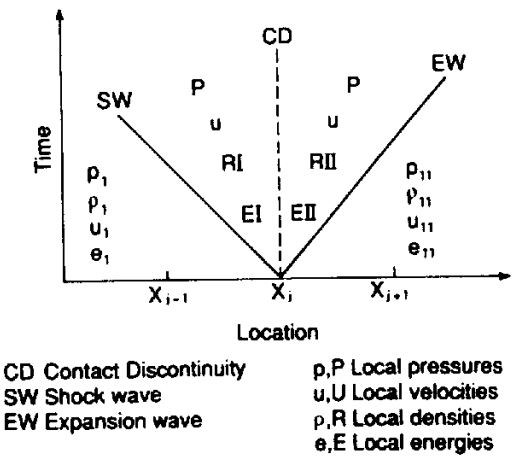

FIG. 4.13. Discontinuity splitting between two gaseous masses.

Figure 13 illustrates the one-dimensional case of a shock wave to the left and an expansion wave to the right. These are usually expressed as follows:

- Left-hand wave:

$$U - u_I + \frac{P - p_I}{\beta_I} = 0 \tag{31}$$

- Right-hand wave:

$$U - u_{II} - \frac{P - p_{II}}{\beta_{II}} = 0 \tag{32}$$

For a shock wave

$$\beta_i = \sqrt{\rho_i \frac{\gamma + 1}{2} P + \frac{\gamma - 2}{2} p_i} \tag{33}$$

where i = I or II, depending on whether the wave is to the left or to the right.

For an expansion wave:

$$\beta_i = \frac{\gamma - 1}{2\gamma} \rho_i a_i \frac{1 - \dfrac{P}{p_i}}{1 - \left(\dfrac{P}{p_i}\right)^{\gamma - 1/2\gamma}} \tag{34}$$

where:

a_i = the sonic speed of the medium $i = \sqrt{\gamma p_i / \rho_i}$

i = I or II, depending on whether the expansion wave is to the left or to the right.

Consequently, the configuration appearing when two gaseous masses come into contact can be determined. Elimination of U between eqns (31) and (32) allows the determination of P solving:

$$F(P) = u_{\mathrm{I}} - u_{\mathrm{II}} = \frac{P - p_{\mathrm{I}}}{\beta_{\mathrm{I}}} + \frac{P - p_{\mathrm{II}}}{\beta_{\mathrm{II}}} = f(P, p_{\mathrm{I}}, \rho_{\mathrm{I}}) + f(P, p_{\mathrm{II}}, \rho_{\mathrm{II}}) \quad (35)$$

with:

$$f(P, p_i, \rho_i) = \begin{cases} \dfrac{P - p_i}{\sqrt{\rho_i \left(\dfrac{\gamma + 1}{2} \cdot P + \dfrac{\gamma - 1}{2} \cdot p_i \right)}} & \text{where } P \geq p_i \\ \dfrac{2}{\gamma - 1} a_i \left[\left(\dfrac{P}{p_i} \right)^{\gamma - 1/2\gamma} - 1 \right] & \text{where } P < p_i \end{cases} \quad (36)$$

The analysis of the function $F(P)$ reveals several possibilities. Assuming that $p_{\mathrm{I}} < p_{\mathrm{II}}$ and writing:

$$F(p_{\mathrm{I}}) = U_{\mathrm{exp}} = -\frac{2a_{\mathrm{II}}}{\gamma - 1} \left[1 - \left(\frac{p_{\mathrm{I}}}{p_{\mathrm{II}}} \right)^{\gamma - 1/2} \right] \quad (37)$$

$$F(p_{\mathrm{II}}) = U_{\mathrm{shock}} = \frac{p_{\mathrm{II}} - p_{\mathrm{I}}}{\sqrt{\rho_{\mathrm{I}} \left(\dfrac{\gamma + 1}{2} p_{\mathrm{II}} + \dfrac{\gamma - 1}{2} p_{\mathrm{I}} \right)}} \quad (38)$$

- If $0 < P \leq p_{\mathrm{I}}$, two expansion waves propagate, one to the left and one to the right. We have:

$$u_{\mathrm{I}} - u_{\mathrm{II}} \leq U_{\mathrm{exp}}$$

- If $p_{\mathrm{I}} < P < p_{\mathrm{II}}$, a shock wave develops to the left and an expansion wave develops to the right. In which case:

$$U_{\mathrm{exp}} < u_{\mathrm{I}} - u_{\mathrm{II}} < U_{\mathrm{shock}}$$

- If $P \geq p_{\mathrm{II}}$, two shock waves propagate, one to the left and the other to the right. In which case:

$$u_{\mathrm{I}} - u_{\mathrm{II}} \geq U_{\mathrm{shock}}$$

The value of P is determined by resolving eqn (35), proceeding by successive iterations using Newton's tangent method which, as indicated by

the authors, ensures a rapid convergence from an initial value. The other parameters are calculated using the P value at convergence [36].

(c) Numerical procedure

Looking at the difference scheme for the unsteady one-dimensional equations of the fluid dynamics developed by Godunov *et al.*, we are provided with a simple illustration of the method. Assuming density ρ, impulse ρu, and total energy $\rho(e + u^2/2)$ constant on each elementary part of the field, the conservation equation laws (described in section 3.2.2) although simplified in terms of the fluid behavior and applied to grid $j - 1/2$ (part $[x_{j-1}, x_j]$) for the period of time from t to $t + \Delta t$, are written as follows:

$$(\rho^{j-1/2} - \rho_{j-1/2})(x_j - x_{j-1}) + \Delta t([RU]_j - [RU]_{j-1}) = 0$$

$$([\rho u]^{j-1/2} - [\rho u]_{j-1/2})(x_j - x_{j-1}) + \Delta t([P + RU^2]_j - [P + RU^2]_{j-1}) = 0$$

$$\left(\left[\rho \left(e + \frac{u^2}{2} \right) \right]^{j-1/2} - \left[\rho \left(e + \frac{u^2}{2} \right) \right]_{j-1/2} \right) + \Delta t \left(\left[RU \left(E + \frac{U^2}{2} \right) + PU \right]_j - \left[RU \left(E + \frac{U^2}{2} \right) + PU \right]_{j-1} \right) = 0$$

Indices in lower position stand for the values at time t while indices in upper position stand for those at time $t + \Delta t$.

The extension of the calculations to three-dimensional configurations can be done: the method used is a finite volume explicit method. The calculations have to be run over a three-dimensional fluid domain discretized in small elementary cells. Within each cell i (volume V_i, surface Σ_i), the conservation equations can be generalized:

$$\frac{\partial}{\partial t} \int_{V_i} (\text{F.F.C.}) \, dV = \int_{\Sigma_i} (\text{F.F.C. flux}) \, d\Sigma \quad (39)$$

where F.F.C. (for flowfield characteristics) is either gas mass density, momentum or energy.

In order to obtain the left-hand term in (39), F.F.C. is assumed to be constant on each basic cell, leading to the following approximation:

$$\frac{\partial}{\partial t} \int_{V_i} (\text{F.F.C.}) \, dV = \frac{V_i}{\Delta t} \left[\text{F.F.C.}_{t + \Delta t, i} - \text{F.F.C.}_{t,i} \right]$$

where $\text{F.F.C.}_{t,i}$ represents F.F.C. at time t over cell i.

To calculate the second term of equality (39) which corresponds to F.F.C. flux through the boundaries of the grid cell, we resolve the contact discontinuity problem with each cell adjacent to cell i using the method described in the previous section.

These calculations are performed in a direction normal to each face of cell i. The tangential components of the velocity are then not modified by crossing a shock or an expansion wave.

This gives the characteristics of the fluid at that boundary: pressure, normal velocity, tangential velocity, mass density and energy. The amplitudes of various fluxes can then be explicitly computed at time $t + \Delta t$ and in cell i using:

$$\text{F.F.C.}_{t+\Delta t,\, i} = \text{F.F.C.}_{t,i} + \frac{\Delta t}{V_i} \int_{\Sigma_i} (\text{F.F.C. flux})\, d\Sigma$$

Equation (39) being completed with the ideal gas state equation, the F.F.C. values at time $t + \Delta t$ can be explicitly calculated, based on the known values at time t and on the "major values" (P, U, R, E) obtained from the discontinuity analysis:

- in two-dimensions, to each of the four faces;
- in three dimensions, to each of the six faces of cell i.

The values of u_I and u_{II} which are taken into account for the calculation at this point are the normal components of the velocity vectors over the boundary selected.

(d) Boundary conditions

The scheme description (eqn 39) shows that boundaries need to be introduced in the form of mass, momentum, and energy fluxes crossing the faces located at the boundary of the computational domain. Further data, depending on the type of boundary met, are necessary to determine these fluxes:

- In the case of an impermeable wall the velocity of the gases penetrating into the cell must be zero at the boundary, i.e. $U = 0$. The determination of P then requires the creation of a phantom cell characterized by the values (u_I, p_I, ρ_I) satisfying the above condition. If (u_{II}, p_{II}, ρ_{II}) are the values of the boundary cell, we see that the selection $u_I^N = -u_{II}^N$ (where the upper index N stands for the component of the velocity vector perpendicular to the face), $p_I = p_{II}$, and $\rho_I = \rho_{II}$ is a solution of the problem.
- If the boundary corresponds to a symmetry plane of the propellant grain, the calculations are handled in the same manner as for the impermeable wall.
- In the case of an injecting wall two steps are necessary to determine the various fluxes. First, the reaction of the wall is calculated as for the inert wall. Second, the fluxes obtained are increased by the mass and energy fluxes resulting from the propellant combustion; the momentum flux related to propellant combustion is assumed to be zero.
- If the boundary is located at the exit plane of the nozzle in the supersonic jet zone, the simplest solution consists in extending the fluid domain a little beyond this plane, and assigning to the phantom cell the same F.F.C. values as those computed for the boundary cell. At the beginning of the calculations, before the nozzle plays its full role, the condition is identical, and consequently not very strict. Care must be taken that the induced error is not spread in the whole internal fluid flow domain.

3.2.4.2. *Examples using the two- and three-dimensional programs*

In Fig. 14 a comparison between the calculated and experimental results is shown for a two-dimensional plane case. The experimental set-up developed by ONERA reproduces a configuration close to the combustion chamber of a nozzleless rocket motor. Its porous walls are fed by a cold air flow (260 K) sufficient to initiate a supersonic regime in the expansion region. Figure 15 illustrates the calculated results for a forehead FINOCYL type of propellant grain.

3.2.5. *Experimental determination of the flowfield*

The tests are performed to:

- determine the flowfield pattern in actual geometries;
- confirm results obtained through predictions. These tests are done on models the geometry of which sometimes differs from the actual propellant grains configurations; nevertheless they have the advantage of an easier control of input parameters and of less complex boundary conditions.

3.2.5.1. *Flowfield measurements*

(a) Pressure measurements

Tests on steady flows do not require the use of transducers having a very wide bandwidth. But to obtain correct measurements of the pressure level in various locations in the flowfield, these pressure gages must be accurate even for fairly high average levels.

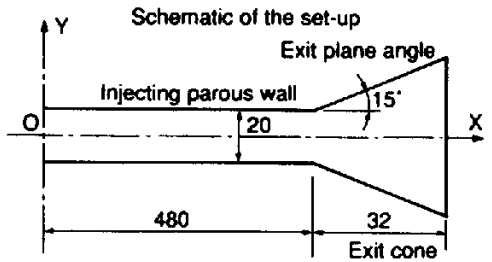

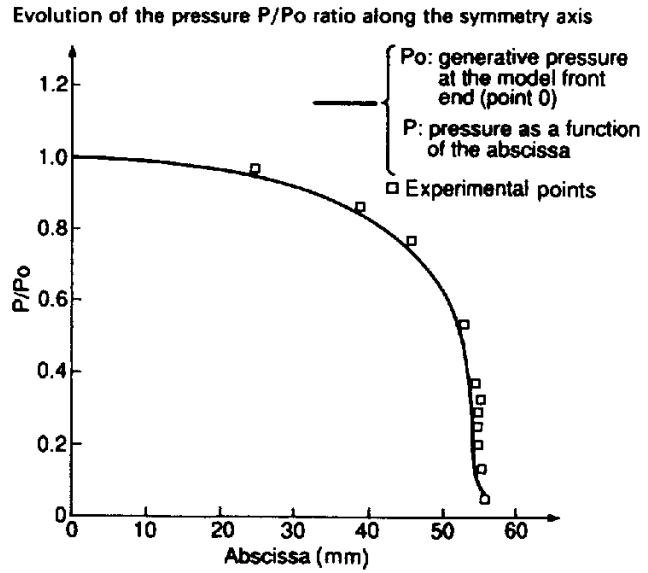

FIG. 4.14. Procne code. Comparison between prediction and experiment.

(b) Velocity measurements

The hot-wire technique [37] used to determine both the average value of the velocity and its fluctuations (needed when evaluating the Reynolds tensor components) is interesting for "clean" flows of cold gases (without particles). Laser anemometry (used by ONERA) allows to examine the local velocity field in cold gases, but it necessitates seeding the fluid with very fine particles.

(c) Temperature measurements

A manufacturing technique for thermocouples of short response time has also been developed. This provides the possibility of measuring temperature in the hot and corrosive gaseous environment of the combustion chamber.

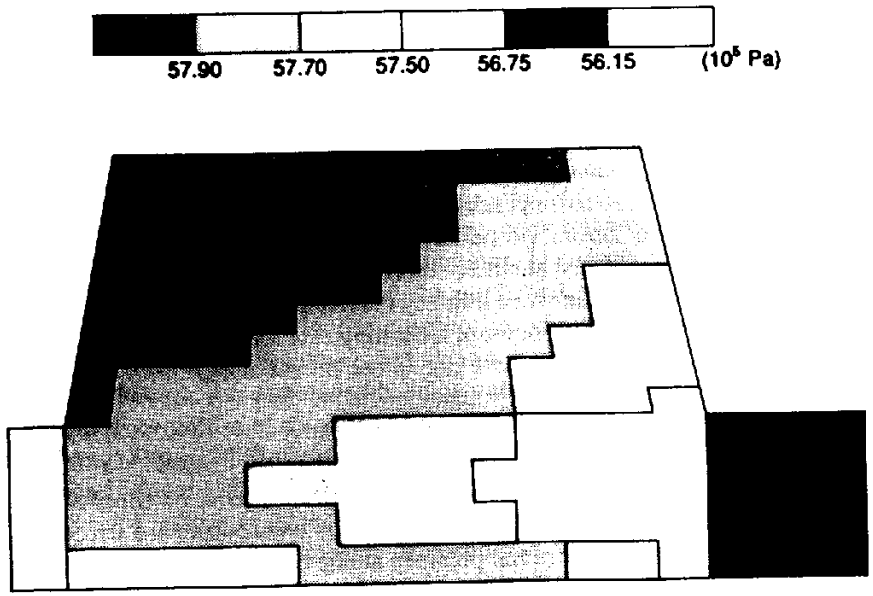

FIG. 4.15. Pressure distribution in a Fin.

(d) Visualizations

Visualization consists of providing a transparent viewport on an experimental set-up in order to observe the flowfield during a test. This process is used with cold and hot gases as well. At very high temperatures it is necessary, however, to make sure that the viewport ablation is not able to distort both the observation of the phenomenon and its progress.

3.2.5.2. Models for the determination of flowfield pattern

(a) Models for analysis of gap pressurization

Free-standing propellant grains exhibit a gap between the thermally insulated metal case and the insulator surrounding the propellant grain. During ignition the pressure inside this gap is not in equilibrium with the presssure in the combustion chamber. Because of this pressure difference, the propellant grain flattens against the case wall, causing an elongation of the propellant grain and the appearance of non-isotropic compression stresses which may affect its structural integrity, particularly in the case of cold firing.

The experimental model is made of a case in which a cylindrical center port propellant grain is placed. The whole assembly is pressurized through an external tank. This is a cold gas test. Numerous gages (pressure, gap

thickness) distributed along various generatrices, describe the model behavior when it is subjected to a pressure rise at a given rate.

(b) Model for streamlines visualization

Several types of geometry can be tested. Figure 16 shows an example of an axisymmetric model. A half-cylindrical propellant grain with axisymmetrical slots, modeling the actual propellant grain configuration, is glued to a viewport. Photographs reveal streamlines issuing from the slots: they experience a significant deviation when meeting the main central spout. In addition, photographs show the occurrence of a burning rate faster at the downstream bottom of the slots than anywhere else in the propellant grain.

(c) Analysis model for pressure field

The propellant grain for these models is axisymmetric, or three-dimensional (FINOCYL). The locations of the various transducers are selected to allow a local measurement of the pressure along the symmetry axes and the burning surface.

The geometry of the chamber is specifically designed so that there are significant pressure differences between the various measurement points. This

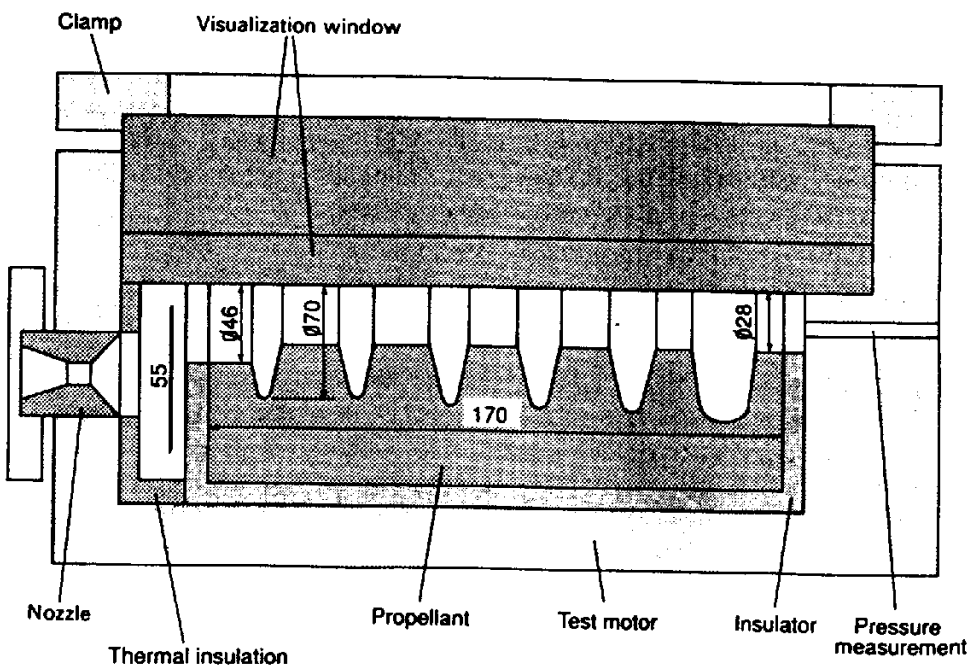

FIG. 4.16. Fluid flow lines visualization during firing of an axisymmetrical test motor. Schematic of the experimental set-up.

also explains why the model is fired under relatively high pressure (approximately 10 MPa), and why, in some cases, it is equipped with a central rod used to increase the pressure differences in the chamber.

3.3. BALLISTICS MODIFICATIONS TIED TO THE INTERNAL AERODYNAMIC FIELD

Performance increases of rocket motors have led to the development of grains with high volumetric loading fractions. The resulting geometries often have the disadvantage of reducing the port areas which, as a consequence, increases the mass flow in the combustion chamber, particularly at the beginning of firing. Experience has shown that, under these conditions, a local increase in the propellant burning rate, causing a deviation from the theoretical evolution of the grain burning surface, occurs at the beginning of the firing. Figure 17 illustrates the evolution of the pressure obtained at the front end of a long star-shaped propellant grain. It clearly shows the existence of an over-pressure at ignition. This phenomenon, which is nowadays better controlled, is sometimes desired to obtain the specified pressure envelope. Considered for a long time to be undesirable, it must be precisely quantified in order to determine its consequences on the structural integrity and the evolution of the propellant burning area.

3.3.1. Erosive burning phenomena

3.3.1.1. Determination of formulation sensitivity

A great number of researchers have developed testing equipment to determine the burning rate of a propellant subjected to a hot mean flux

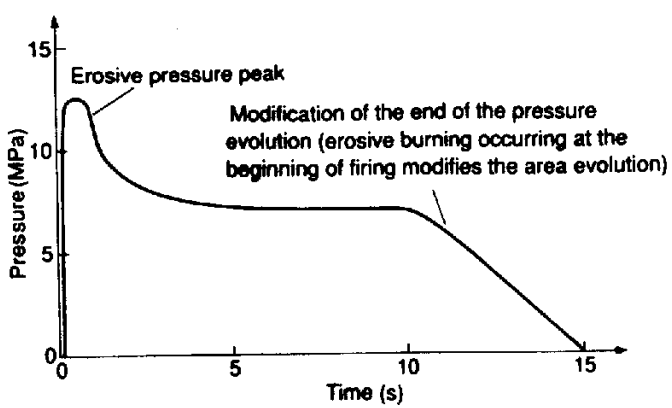

FIG. 4.17. Erosive burning of a star-shaped grain, diameter 203 mm, length 1000 mm.

parallel to its burning surface. Most of them used small test samples, shaped like small thin plates, placed in the hot gas flow released by a gas generator located upstream.

Various methods have been used to determine the burning rate of the sample: X-ray photography, detection of the burning time through a photomultiplier, extinction to pattern the new surface of the partially-burned sample, and high-speed photography through a transparent viewport.

Published research describes various set-ups. Razdan and Kuo [38], and King [39] used a gas generator, placed upstream. In France, at ONERA and SNPE, interesting test systems have been developed, based on the use of the ultrasonic method. This method allows a direct and local measurement of the burning front location and therefore, by differentiation, the rate of propellant burning rate without perturbing the phenomenon. This system is illustrated in Fig. 18; it includes a viewport making it possible to use several ultrasonic transducers, as well as the use of large quantities of propellant. The latter characteristics offer the advantage of conditions closer to the actual combustion of propellant grains, without having to resort to a gas generator.

3.3.1.2. Experimental results

The most important observations are [38]:

- The occurrence of an erosive phenomenon related to a threshold value of the main flow. It is possible, for a large number of compositions, to

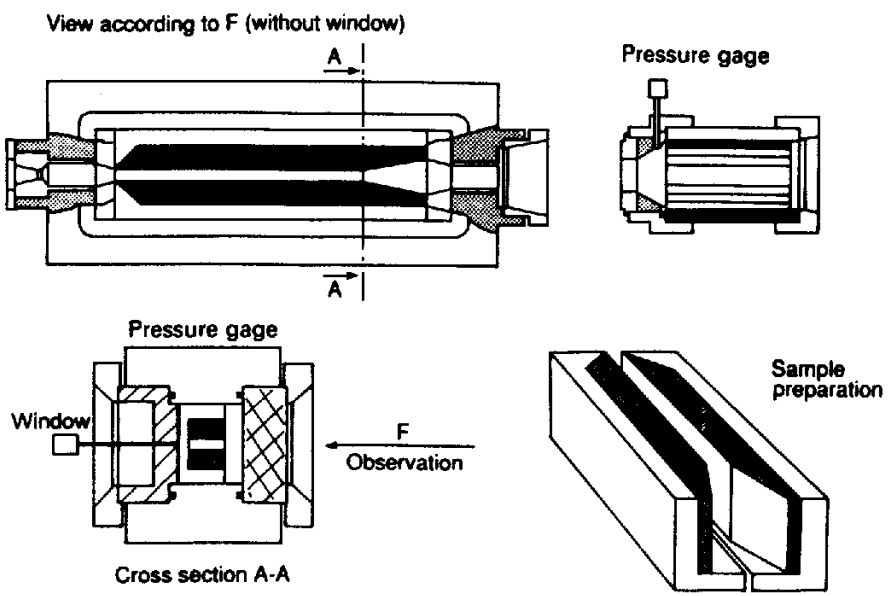

FIG. 4.18. Erosive burning experimental arrangement.

determine one velocity threshold (or specific mass flow rate) beyond which the propellant burning rate increase occurs. The lower the reference burning rate (value determined when there is no mean flow) the greater its sensitivity to the main flow will be.

- For a given flow velocity the propellant sensitivity depends on the pressure level. The experiments performed by Marklund and Lake [40] show that, for the same flow velocity at the walls, the relative burning rate increase grows with the pressure level. But if we consider the specific mass flow rate instead of the flow velocity, we still find the trends previously noticed with the variation of the propellant reference burning rate. The higher the pressure, the faster the reference burning rate of the propellant which then becomes less sensitive to the specific mass flow rate.
- Typically, the main flow temperature and chemical species have no effect:
  - the sensitivity of a propellant composition is independent of the nature of gases produced by the generator when the combustion gases are non-reactive;
  - the burning rate increase seems basically independent of the temperature of the hot gases sweeping the propellant surface.
- The presence of certain formulation parameters may lead to a negative erosive effect: this effect (burning rate decrease instead of increase) is clearly observed with active binder compositions the basic burning rate of which has already been increased by a ballistic modifier. Several possible explanations are offered:
  - decrease of the heat transfer at the surface caused by a "blowing" of the chemical reactants in the boundary layer that modify the transmission coefficients and the reaction rates:
  - formation of a melt binder coating on the surface, caused by the shear stress in the fluid;
  - in some cases, destruction of the carbonized residue due to the addition of ballistic modifiers in the propellant composition.

3.3.2. Modeling of the phenomenon

3.3.2.1. The basic models

To relate the value of the local burning rate to the gas flow characteristics in the combustion chamber, various empirical or theoretical laws have been advanced.

(a) The multiplicative law

$$r = r_b(1 + ku) \quad \text{or} \quad r = r_b(1 + kG) \tag{40}$$

where:

$r_b = ap^n$ = reference burning rate of the composition;
k = constant;
u = average velocity of the main flow, assumed to be one-dimensional;
$G = \rho_g u$ = specific mass flow rate of the main flow;
ρ_g = density of the gases.

Likewise, with the introduction of a G^* threshold of flow rate:

$$r = r_b[1 + k(G - G^*)] \tag{41}$$

Green and Vilyunov proposed similar equations [40].

(b) The additive law

This type of law, expanded from research work done by Corner and Geckler, was proposed by Boisson [41]:

$$r = r_b + ku \tag{42}$$

3.3.2.2. Detailed models

(a) Lenoir and Robillard model

Lenoir and Robillard [42] propose a description of the erosive mechanism where the burning rate increase results from the heat transfer from the flow to the burning surface. For a given pressure and an external flow, the new propellant burning rate is calculated by adding an erosive component to the reference burning rate. It is obtained from the energy equilibrium at the surface:

$$\alpha(T_f - T_s) = \rho_p r_e[L + c_p(T_s - T_i)] \tag{43}$$

where:

r_e = erosive burning component;
L = heat resulting from the decomposition of solid into gas, assumed null by Lenoir and Robillard;
T_f, T_s, T_i = respectively, flame, surface and initial temperature of the propellant;
c_p = propellant specific heat;
ρ_p = propellant density.

The coefficient of heat transfer α is the Chilton–Colburn coefficient modified by Rannie [41]. It accounts for the surface injection:

$$\alpha = 0.0288 \cdot c_g \cdot \rho \cdot u \cdot R_{ex}^{-0.2} \cdot P_r^{-2/3} \cdot \exp\left[-\beta \frac{\rho_g \cdot v_g}{\rho u}\right] \tag{44}$$

where:

c_g = specific heat of the gases at constant pressure
R_{ex} = Reynolds number, based on the axial position
ρ, u = respectively, density and velocity of the main flow
ρ_g, v_g = respectively, density and velocity of the gases emitted at the injecting wall
β = constant
P_r = Prandtl number

Taking eqns (43) and (44) into account, the new burning rate is implicitly expressed by:

$$r = ap^n + r_e \tag{45}$$

Some researchers [38] have modified this law:

- using a Reynolds number based on the diameter rather than on the axial location;
- introducing a term representing the mechanical erosion (Osborn and Burick);
- introducing, for catalyzed EDB formulations, an additional component due to the plateau effect when it exists (constant burning rate whatever the pressure level): Jojic and Blagojevic.

(b) Analytical models for boundary layer including the burning mechanisms

Lengellé's model [43]

The basic burning model used is Summerfield's GDF model, which is representative of composite propellant containing ammonium perchlorate. With this model, which only takes into account a diffusion flame between the oxidizing products (AP decomposition) and the combustible gases (binder decomposition), and assuming the Lewis and Schmidt numbers to be close to one, the burning rate is given by:

$$r = \left[\frac{c_g(T_f - T_s)}{Q}\right]^{1/2} \cdot \frac{\rho_g}{M^{1/3}} \cdot \frac{\mu}{\rho_p}\left(1 + \frac{\rho \cdot \varepsilon}{\mu}\right) \tag{46}$$

where:

c_g = specific heat of gases;
T_f, T_s = respectively, flame and surface temperatures;
Q = energy necessary to heat the propellant and transform it into gas;
ρ_g, ρ_p = respectively, gas and propellant density;
M = mass of a pocket of combustible gas;

μ, ε = coefficients representing, respectively, viscosity and turbulent diffusion in the main flow.

Expression (46) was established taking into account the modification of the transport properties of the fluid by the main flow. Consequently, the GDF model leads to add to the reference burning rate of the composition, a term related to the local flow pattern, as the height of the flame itself is not affected.

The term $\rho \cdot \varepsilon/\mu$ in (46) is calculated from the integration of the equations within a Couette flow boundary layer assuming a constant external velocity independent of the downstream location. Based on the work of Marxman, Lengellé writes the equation that gives the velocity profile (inside the boundary layer) above a plane plate with a constant injection velocity at the wall. Based on this profile, on the calculation of the momentum thickness, and on the friction coefficient, Lengellé calculates the turbulent diffusion term using Prandtl's mixing length assumption. This term changes within the bounday layer. Lengellé suggests using its average value for the entire flame height L. The relationship providing the propellant burning rate is written as follows:

$$r = \frac{c_g}{\rho_p}\frac{(T_f - T_s)}{Q}\left[\frac{\mu}{L} + \frac{8.3}{10^2}\frac{\rho_e \cdot \mu_e}{R_{ex}^{0.1}}\left(\frac{L}{\delta}\right)^m \psi\right] \tag{47}$$

where:

$$\psi = \frac{\ln(1+B)}{B}\left[1 + B\left(\frac{L}{\delta}\right)^\alpha\right]\frac{1}{\alpha+2}$$

King's model [44]

The mechanisms considered in this model are also representative of composite propellants combustion, containing ammonium perchlorate. Two flames are included:

- the premixed flame of the ammonium perchlorate, considered as a monopropellant;
- the diffusion flame between the gaseous species produced by AP and binder decompositions.

The burning rate, determined by the energetic balance at the surface, is then given, without external flow by:

$$r = \frac{I}{\rho_p \cdot Q}\left[\frac{\lambda_1(T_{fox} - T_s)}{L_f} + \frac{\lambda_2(T_f - T_s)}{L_{diff} + L_{kin}}\right] \tag{48}$$

where:

ρ_p, Q = same definitions as for (46);
λ_1 = thermal conductivity of the $HClO_4/NH_3$ gaseous phase;
λ_2 = thermal conductivity of the oxidizers/fuels mixture issued from AP and binder decomposition;

T_{fox} = AP flame temperature;
T_f = diffusion flame temperature;
T_s = propellant surface temperature;
L_f = AP flame height;
L_{Diff}, L_{Kin} = parameters related to diffusion flame, respectively: height due to the diffusion and to kinetics of reactions.

When expressing the various heights, King writes:

$$r = A_1 p\left\{1 + \frac{A_2}{1 + A_3 p^2 d_{AP}^2}\right\} \tag{49}$$

where:

A_1, A_2, A_3 = constants depending on propellant and gases thermal properties and on the propellant surface temperature and heights corresponding to the various flames types;
p = pressure;
d_{AP} = diameter of AP particles

In this model the action of the flow is taken into account through the diffusion flame bending under the effect of fluid velocity; eqn (48) becomes:

$$r = \frac{1}{\rho_p \cdot Q}\left[\frac{\lambda_1(T_{fox} - T_s)}{L_f} + \frac{\lambda_2(T_f - T_s)}{L_{Diff} \cdot \sin\theta + L_{Kin}}\right] \tag{50}$$

where $\theta(<\pi/2)$ is the angle formed between the diffusion flame axis and the burning surface.

The various physical properties used in eqn (50) keep the same value in the case of an injecting wall. Angle is calculated from the velocity profile in the boundary layer using a simple iterative process. Empirical equations, based on Mickley and Davis' experimental results, make it possible to express the local fluid velocity as a function of transverse location above the propellant surface, main flow velocity and velocity of the injected gases.

(c) Recent models

These models (Sviridenkov and Yagodkin in 1976, Razdan and Kuo [38], Beddini [45]) solve the conservation equations for simple two-dimensional configurations (plane plates, cylindrical channels) of constant port area. Far from the wall, simplifying assumptions are considered [38]: the two-dimensional flow is isentropic and the fluid is non-viscous, though this assumption was not invoked in ref. [45].

Close to the wall the fluid behavior is more complex; terms related to viscosity are included (taking into account the Reynolds tensions). These researchers use the assumption that a turbulent flow field, when averaged, is

steady: each physical parameter consists of an average steady value and of a term representing the fluctuation from the average value over time.

3.3.2.3. *Practical applications*

The so-called "standard grain" SNPE method was developed for the purpose of a quick determination of the propellant erosive burning sensitivity. It consists of firings at fixed pressure of small star-shaped grains. These tests are performed on grains of various length, therefore corresponding to an evolution of the burning surface area to the port area ratio. Approximate values of the erosive burning parameters of the composition tested (slope k and threshold G^* of eqn 41) are worked out applying King's model [44], when the propellant is a composite containing ammonium perchlorate. The values are later refined to match as best as possible the pressure evolution (Fig. 19).

4. Transient and Unsteady Burning Phenomena

In the previous sections the mechanisms involved during steady burning or slowly evolving operation sequences of a solid propellant rocket motor were discussed. On the contrary, the following section deals with phenomena observed during transient or unsteady burning: ignition and burn-out periods, unexpected development of pressure oscillations in the combustion chamber or thrust modulation.

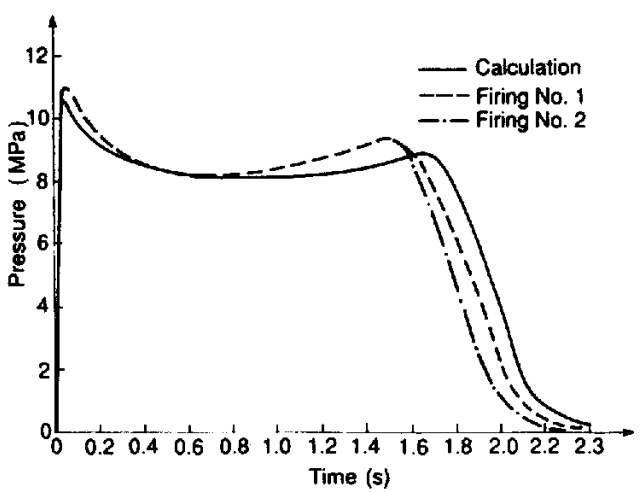

FIG. 4.19. Comparison between prediction and experiment. Using the first King's model.

4.1. TRANSIENT BURNING

4.1.1. *Origin*

Transient burning occurs when the pressure level in the combustion chamber changes very rapidly with time. Assuming a stationary regime (Section 2.2), the heat flux transmitted by the gaseous phase creates a thermal gradient in the propellant close to the burning surface. The equilibrium displacement caused by any pressure variation requires an adjustment of thermal gradients in the gaseous and condensed phases. Characteristic times are associated with each zone:

for the propellant:

$$\tau_p = \frac{d_p}{r^2} \tag{51}$$

for the gaseous phase:

$$\tau_g = \frac{\lambda_g \cdot c_p \cdot \rho_g}{\lambda_p \cdot c_g \cdot \rho_p} \cdot \tau_p$$

where:

λ_i, c_i, ρ_i are, respectively, thermal conductivity, specific heat, and density of the propellant (index p) and of gas (index g) at constant pressure

d_p is the propellant heat diffusivity

The typical residence time associated with the gaseous phase is much smaller than the corresponding time for that associated with the solid propellant. Consequently, several cases may occur, depending on the time during which the pressure level is changed.

- if $\tau \ll \tau_p$ no unsteady effect;
- if $\tau \approx \tau_p$ the thermal gradient evolution in the propellant is delayed while the gaseous phase instantaneously adjusts itself to pressure changes;
- if $\tau \approx \tau_g$ each burning mechanism is affected by the fast pressure evolution.

4.1.2. *Models*

Kuo *et al.* [46] have done a very clear presentation of the conservation equations that need solving to deal with the general problem of unsteady burning. Various types of models have been developed. They significantly differ from each other by:

- the terms excluded or included in the conservation equations;
- the method selected to solve the governing equations.

4.1.2.1. *Models of dp/dt type* [47,48]

The gaseous phase of these models is assumed to be steady and the unsteady heat equation resolution is simplified. These models provide the following relationship for the instantaneous burning rate:

$$r = r_b\left[1 + \psi\left(\frac{n \cdot d_p}{p \cdot r_b^2}\right)\right]\frac{dp}{dt} \tag{52}$$

where:

$r_b = ap^n$ = steady-state burning rate;
d_p = propellant thermal diffusivity = parameter which depends upon instantaneous pressure and propellant characteristics.

4.1.2.2. *Zel'dovich–Novozhilov model*

Zel'dovich [49] assumes that during the unsteady regime the gaseous phase instantly reacts. The heat flux at the propellant surface is found from the steady analysis of propellant regression, avoiding a detailed and tricky modeling of the gaseous flame zone.

Equation (3) gives the expression of the steady-state temperature profile occurring in the propellant assuming no condensed phase reaction. The value of the surface heat flux is then:

$$\Phi_{p,s} = \lambda_p \left.\frac{dT}{dx}\right|_{x=0^-} = \frac{r_b \cdot \lambda_p}{d_p}(T_{s,s} - T_i) \tag{53}$$

where:

$\Phi_{p,s}$ = heat flux at the propellant surface;
λ_p = propellant thermal conductivity;
d_p = propellant thermal diffusivity;
$T_{s,s}$ = propellant surface temperature for the steady-state regime;
r_b = propellant stationary burning rate.

In addition, the steady-state propellant pyrolysis and burning rate laws (eqn 4), are assumed to be valid and the convenient relationship between surface temperature, initial temperature, pressure and burning rate is then established. The heat conservation equation relative to unsteady events can now be solved by including the steady-state thermal flux expression at the propellant surface using stationary data. Due to assumptions involved, this method is not suitable for homogeneous propellants.

4.1.2.3. *Models with flame zone description*

These models [47,50] solve the conservation energy equations for the gaseous zone to determine the heat flux value at the propellant surface. Simplifying assumptions are used; combustion, in particular, is represented by only one reaction. Assuming a uniform production rate for the flame products, the KTSS model [47], used for heterogeneous propellants containing AP (diffusion flame), gives the following value for the unsteady heat flux at the propellant surface:

$$\Phi_{g,s} = -\lambda_g \left.\frac{dT}{dx}\right|_{x=0^+} = \frac{1}{r} \cdot \rho_p \cdot r_b^2 \left\{c_p\left[\frac{r_b}{b}\right]^{1/k} - Q_s\right\} \tag{54}$$

where:

r = instantaneous burning rate;
r_b = stationary burning rate = ap^n;
c_p, ρ_p = respectively, propellant specific heat and density;
b, k = steady-state pyrolysis law coefficients written as $r_b = b(T_{s,s} - T_i)k$;
Q_s = heat released by the superficial decomposition reactions.

4.2. IGNITION

4.2.1. *Propellant grain ignition — flame spreading*

A pyrotechnical device is used to ignite the propellant. Hot gases and particles supplied by the igniter heat the propellant surface by conduction, convection and thermal radiation. This heat flux is sufficient for the propellant surface to ignite in some scattered spots. Then the flame propagates, the combustion reactions begin to be self-sustained, and the entire surface is soon burning.

Equation (12) under certain assumptions expresses the pressure rise due to the central bore gas filling, consequence of the propellant surface ignition. When written as:

$$\ln\left\{\left[1 - \left(\frac{p_c}{p_{co}}\right)^{1-n}\right]^{-1}\right\} = \frac{1-n}{t_s} \cdot t \tag{55}$$

the left-hand side term becomes a linear function of time t. This offers the possibility, together with pressure recordings to determine the flame propagation time [51]. It also allows one to calculate the maximum pressure rise in the chamber,

$$\left.\frac{dp_c}{dt}\right|_{max} = \frac{p_{co}}{t_s}(1-n)n^{n/(1-n)} \tag{56}$$

This equation demonstrates that, theoretically, the smaller n, the greater the pressure rise.

The rate of flame speed is particularly important when the propellant grain is very long, or when the internal configuration is complex. Barrère [52] has worked out an equation for convective heat transfer to the propellant surface.

4.2.2. Experimental methods for ignition study

The ignition characteristics of the various propellant families are usually determined by performing tests on small samples. Hermance [53] has reviewed the various methods used.

(a) Ignition through conductive heat transfer

As a reminder, numerous experiments are conducted in a shock tube. In this technique the propellant sample ignites under the sudden pressure and temperature rise resulting from the shock wave.

(b) Ignition through convective heat transfer

Lengellé *et al.* [54] describe a set of results obtained by submitting a sample to hot gases produced by either an arc generator or a small motor using a polybutadiene solid propellant.

(c) Ignition through radiative flux

At present the laser beam method is widely used. A CO_2 laser, emitting a 10.6 μm coherent beam and about 200 W cm^{-2} flux, is well suited for the propellant ignition studies. This technology offers the possibility of selecting a flux level independent of pressure level, chemical nature of ambient gases and moisture level. In addition, the laser can be operated in a pulsed mode. It is then possible to differentiate the self-sustained combustion sequence occurring after ignition from possible dynamic extinguishment. However, the laser ignition method has several drawbacks:

- absence of hot gases at the sample surface;
- sometimes deep beam penetration inside the propellant;
- a relatively slow increase of the surface temperature in comparison with actual ignition events.

4.2.3. Thermal flux measurement [56]

The flux received by a surface can be total or selective:

- to determine the total incident flux, the fluxmeter emissivity is, as much as possible, close to one;
- to determine the flux actually received by the surface, the fluxmeter emissivity matches the propellant one;
- to select radiative flux, a viewport is placed between the fluxmeter and the heat source: its spectral characteristics are chosen to allow a good transmission of the source radiant component and it also plays the role of a protection against convective flux.

4.2.4. Characterization of the various propellant families

4.2.4.1. Ignition delay—flux charts

Before ignition, the unsteady heat equation can be solved if the initial temperature $T(x, 0)$ or flux $\Phi(x, 0)$ fields are known. This equation is written:

$$\frac{\partial T}{\partial t} = d_p \frac{\partial^2 T}{\partial x^2} \qquad x \le 0, \quad 0 \le t \le t_{ign} \tag{57}$$

where t_{ign} is the ignition delay under constant flux.

In the particular case where a propellant (initial uniform temperature T_i) is ignited, and assuming that its thermal properties are independent of the instantaneous local temperature, the following equations are obtained:

$$T_s(t) - T_i = \frac{1}{\sqrt{\Gamma \pi}} \int_0^t \Phi(\tau) \frac{d\tau}{\sqrt{t - \tau}} \tag{58}$$

$$\Phi(t) = \sqrt{\frac{\Gamma}{\pi}} \int_0^t \dot{T}_s(\tau) \frac{d\tau}{\sqrt{t - \tau}} \tag{59}$$

where:

T_s = propellant surface temperature;
$\dot{T}_s = dT_s/dt$;
Φ = flux incident to the propellant surface = $\lambda_p \, dT/dx|_0$;
t = time;
Γ = propellant thermal effusivity;
T_i = propellant initial temperature.

When the tests are performed under constant flux level, eqn (58) becomes simpler:

$$T_s(t) - T_i = \frac{2}{\sqrt{\Gamma \pi}} \Phi \cdot t^{1/2} \tag{60}$$

Representing surface temperature rise of the heated propellant, eqn (60) is further verified during ignition:

$$T_{s,ign} - T_i = \frac{2}{\sqrt{\Gamma\pi}} \Phi \cdot t_{ign}^{1/2} \qquad (61)$$

where $T_{s,ign}$ is the propellant surface temperature at ignition.

If, for a given propellant, ignition occurs at the same surface temperature ($T_{s,ign}$), regardless of the flux level, experimental results must align in the ($T_{s,ign}$ – ln Φ) axis with a (–1) slope value. Figure 20 shows that eqn (61) is clearly verified, whatever the propellant family; but it must be pointed out that the higher the ignition delay the lower the ignition temperature.

4.2.4.3. Modification of the ignition delay — flux charts

(a) Definition of the ignition delay (Fig. 21)

Under an external heat flux the propellant starts to decompose. The regression of its surface is observed. This event sometimes occurs simultaneously with a luminous reaction taking place even before the conditions for sustained ignition are met (concentration of reactants, thickness of the propellant heated zone). At this moment a sudden suppression of the external flux leads to drastic extinguishment.

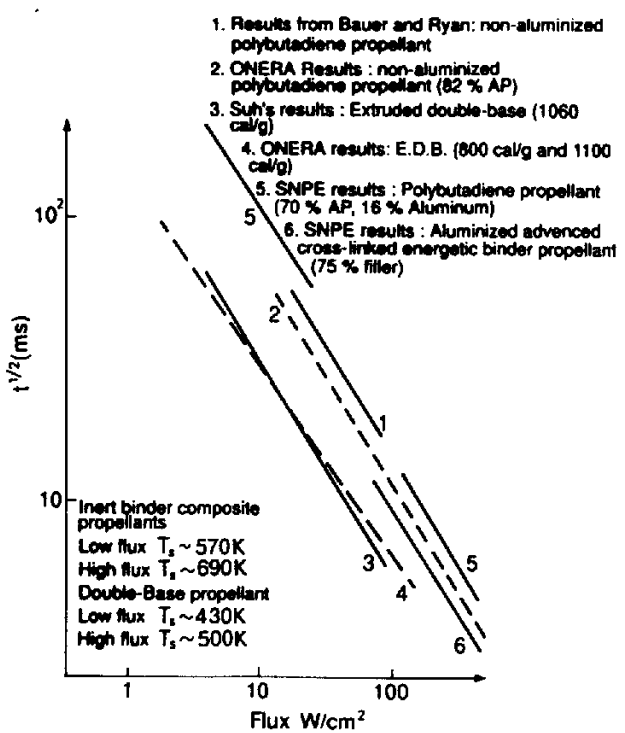

FIG. 4.20. Ignition chart for different propellant families. Tests performed with CO_2 laser under continuous radiation.

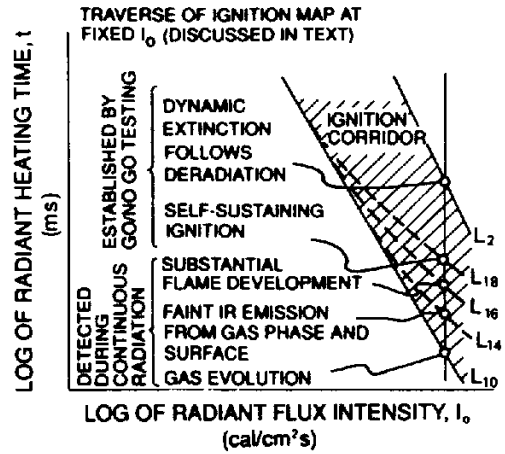

FIG. 4.21. Different events occuring during ignition.

Flux pulses of variable duration are used with the "go/no go" technique to obtain ignition maps and delimit the self-sustained burning region (L_{1d} point) on the delay-flux chart.

(b) Definition of a dynamic extinction region

Experiments performed on double-base propellants containing no ballistic catalysts [58] have shown that, a long time after ignition, the propellant may be extinguished by suppressing the external flux. These experiments demonstrate the existence of a dynamic extinction limit, thereby determining a region on the "ignition delay-flux" map where the combustion is self-sustained after flux suppression (Fig. 21). They also show that this extinction limit greatly depends, as opposed to the ignition limit, on the pressure level: the higher the pressure, the larger the self-sustained combustion region. De Luca [59] believes that this behavior can be generalized to all propellants.

(c) Effect of flux source

Several authors have published experimental results showing that the nature of the flux has no noticeable influence on ignition events, provided that:

- an effective flux is taken into account during tests performed under convective flux, because of the flux level variation during propellant heating;
- radiation penetration in the propellant is limited during radiative flux tests.

(d) Effect of optical properties

Because propellant is not entirely opaque, a portion of the incident radiation is absorbed deep inside the solid, thereby increasing the ignition delay [60].

(e) Effect of pressure level

Although it does not influence the ignition delay value when the flux intensity is low ($< 10\ W \cdot cm^{-2}$), pressure variations significantly modify the previous charts under high thermal fluxes: whatever the propellant family, the higher the pressure, the lower the ignition delay.

(f) Effect of oxygen partial pressure

Experiments reported by Hermance [53] show that the ignition delay decreases when the oxygen partial pressure increases. It appears that, with low concentrations of oxygen, the binder nature has a significant influence.

4.2.5. Numerical simulations

Under a forced constant flux, and considering an initial temperature field evenly distributed, numerical models can predict the surface temperature profile before and after ignition, until a steady-state combustion regime has been reached. The propellant surface regression is introduced into the governing equations as soon as its surface temperature reaches a critical value.

One of these codes, developed by ONERA, has been adapted for extruded double-base propellants. A description of condensed phase reactions and stationary primary flame is included. Another code has also been developed for polybutadiene propellants. The Zel'dovich-Novozhilov method is used to compute the incident flux at the propellant surface.

4.3. INSTABILITIES IN SOLID ROCKET MOTORS

4.3.1. Background

Combustion instabilities during a rocket motor operation are detected as oscillations superimposed to the average pressure. Their amplitude depends on the firing conditions and they are always undesirable, even if they do not all have catastrophic consequences:

- average pressure shifts modify the motor performance, including exceeding specified limits; they sometimes lead to motor failure;
- heat transfers are intensified by pressure oscillations and induce such a rapid degradation of inner parts (thermal insulation, nozzle) that in some cases they are destroyed before burn-out.
- pressure oscillations create vibrations which are transmitted to the whole motor case causing greater stress on it than expected.

4.3.1.1. Origin of motor instabilities

The existence of numerous perturbation sources inside a combustion chamber (small solid pieces ejected by the nozzle, inner jets confluence, etc.) may be at the origin of the combustion instabilities. These perturbations affect propellant combustion. The burning rate adjustment to the instantaneous pressure value triggers an oscillatory phenomenon, the frequency of which may be close to one of the acoustic modes of the central port acting as a resonant cavity. They can also be close to frequencies specific to the internal flow pattern. Instabilities occurrence and feeding in a rocket motor are due to the energetic balance between amplifying (combustion) and damping (condensed phase in gases, case vibrations, etc.) phenomena.

4.3.1.2. Classification of instabilities

Two sets of phenomena are referred to as "instabilities."

(a) Irregular combustion phenomena

Pressure oscillations, even extinction and reignition are observed. These oscillations, of a few hertz, are in phase throughout the whole combustion chamber. They are called "chuffing" or "L*", or "non-acoustic low frequency" instabilities (NALF). They occur under very specific operating conditions: at low pressure and small characteristic length L^* (combustion chamber volume to throat nozzle area ratio).

(b) Pressure oscillations matching cavity acoustic modes:

Two families of instabilities are observed:

- Longitudinal instabilities, matching the longitudinal modes of the cavity. They are characterized by frequencies of a few hundreds of hertz and moderate peak-to-peak amplitudes, sometimes associated to average pressure shifts. They are typically observed on large rocket motors.

- Transverse instabilities, following the transverse modes of the cavity (in a cross-section of the cavity); these are characterized by frequencies of a few tens of kHz, high peak-to-peak amplitudes and generally sudden and important average pressure shifts. They occur on small rocket motors using non-metallized propellants.

4.3.1.3. Determination of acoustic modes

Acoustic pressure field description is needed to predict instabilities occurrence. The wave equation is solved using classical acoustics assumptions [33]:

(a) oscillation p' has a low amplitude compared to average pressure p;
(b) absence of average flow;
(c) walls are rigid (the nozzle is acoustically closed):

$$\frac{\partial^2 p'}{\partial t^2} - \bar{a}^2 \cdot \Delta p' = 0 \quad (\text{where } \bar{a} = \text{average speed of sound})$$

with the following boundary conditions:

$$\vec{\nabla} p' \cdot \vec{n} = 0$$

Computations in the case of simple geometries

When considering a closed tube as a first approximation of a simple motor cavity, the solution is expressed by:

$$p' = p(r, \theta, z) \cdot \cos(\omega t + \psi)$$

where $p(r, \theta, z)$ represents the spatial distribution of the mode (now shortened as $\hat{p}$).

For a stationary mode, we have:

$$\hat{p} = A \cdot J_m\left(\frac{\pi \cdot \alpha_{mn} \cdot d}{D}\right) \cdot \cos(m\,\theta + \varphi) \cdot \cos\left(\frac{\pi q z}{L}\right) \qquad (62)$$

and

$$f = \frac{\omega}{2\pi} = a\sqrt{\left(\frac{\alpha_{mn}}{D}\right)^2 + \left(\frac{q}{2L}\right)^2};$$

L = length of the cavity;
D = port diameter;
d = considered diametral position;
a = average speed of sound in the gases;
m, n, q = arbitrary integers;
J_m = Bessel function of mth order;
α_{mn} = roots of $dJ_m/dr = 0$ (tabulated values);
φ, ψ = phase angles;
A = amplitude known with a multiplicative constant.

Modes can be classified depending on m, n and q values:

$m = 0 \quad n = 0 \quad q \neq 0$ pure longitudinal mode
$m \neq 0 \quad n = 0 \quad q = 0$ pure tangential mode
$m = 0 \quad n \neq 0 \quad q = 0$ pure radial mode

Computations in the case of complex geometries

In the case of actual more complex propellant grain configurations (machined grains or FINOCYL), longitudinal and transverse modes are obtained by specific computer programs solving the wave equation in the combustion chamber. Figure 22 illustrates this type of resolution for a grain with axisymmetric slots; longitudinal acoustic modes are determined using a finite elements procedure.

4.3.2. Unsteady combustion models

4.3.2.1. Definitions

The purpose of this section is to identify the sensitivity of the propellant combustion to the acoustic field ("pressure-coupling" effects) and to the aerodynamic field ("velocity-coupling" effects).

Pressure-coupling

The propellant pressure-coupled response involves two major effects:

(a) mass flow rate response to pressure fluctuations:

$$R_{MP} = \frac{m'/\bar{m}}{p'/\bar{p}}$$

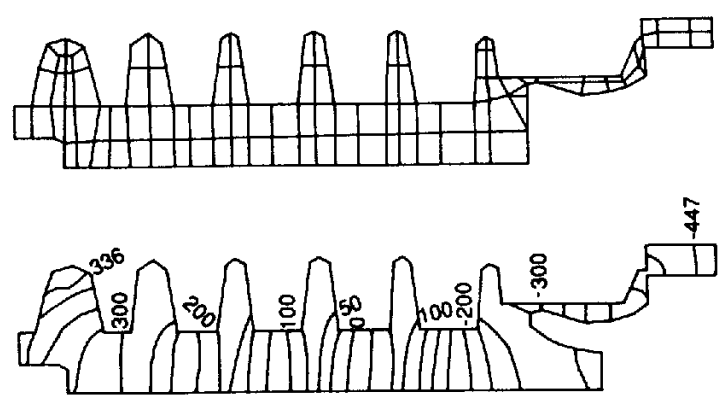

FIG. 4.22. Axisymmetric propellant grain analysis. Grid and isopressure values.

(b) mass flow-rate response to temperature fluctuations:

$$R_{TP} = \frac{T'/\bar{T}_f}{p'/\bar{p}}$$

where:

m', p', T' are respectively maximum specific mass flow rate, pressure and temperature fluctuations;
$\bar{m}$,$\bar{p}$, $\bar{T}_f$ are respectively average values of specific mass flow rate, pressure and flame temperature.

Fluctuations are mainly dependent on frequency and average pressure. If the frequency is very low, specific mass flow rate response term is equal to the pressure exponent of the steady-state burning rate law.

Velocity-coupling

In the linear range the specific mass flow rate response is defined by:

$$R_{MV} = \frac{m'/\bar{m}}{u'/\bar{a}}$$

where:

u' = unsteady normal component of gas velocity;
$\bar{a}$ = average speed of sound.

The velocity-coupling phenomenon is complex, depending on the average velocity of combustion gases and acoustic velocity fluctuations. Unlike pressure-coupling, the velocity-coupled response is not only a propellant characteristic, since it also depends on the gas flow pattern inside the chamber.

4.3.2.2. *Models*

Current models are one-dimensional and based on a description of the combustion zone. Simplifying assumptions especially involve a homogeneously heated solid phase, a very small interface where the decomposition reactions occur and a gaseous phase where combustion products react. The following expression for the specific mass flow rate response has been proposed by Culick [61]:

$$R = \frac{n \cdot A \cdot B}{\lambda + (A/\lambda) - (1 + A) + A \cdot B}$$

where:

λ = complex function of frequency f;
n = exponent of the steady-state pressure law $r = ap^n$;
A and B = constants, worked out from physicochemical analysis (activation energies, surface temperature).

4.3.3. *"L*" instabilities*

This chuffing phenomenon is characterized by pressure oscillations at very low frequencies (a few hertz). Large pressure peaks and depressions are generally observed:

- the amplitudes of pressure oscillations are inversely proportional to the frequency;
- frequency increases with pressure;
- an increase of the motor characteristic length (L^*) leads to a decrease of frequency and of oscillations magnitude.

For the moment, only experimental methods enable the designer to predict motor L^* instabilities occurrence.

4.3.4. *Prediction of instabilities*

4.3.4.1. *Background*

Due to the complexity of phenomena, the methodology of instabilities prediction has been split in two major steps:

- The first step is devoted to predict instability risks; it consists in determining whether a perturbation will tend to grow (unsteady operation) or damp (steady-state operation); this analysis must be made for each potential mode.
- The second step is run for each unstable mode. It consists in computing limiting cycles amplitude as well as the magnitude of average pressure shift. Theoretical approaches account for non-linear phenomena that, in this case, drive instabilities growth.

4.3.4.2. *First step: linear acoustic balance*

Linear acoustic balance theory

Linear acoustic balance is the most widely used approach. The principles of this method have been given and developed by Culick [62].

The fluid mechanics equations, written for the combustion chamber, and the ideal gas state equation are linearized: small quantities, called "perturbation parameters" such as the Mach number and the amplitude of the pressure oscillations, are the new unknowns. The problem consists of seeking solutions expressed in the following form:

$$p' = \hat{p} \cdot \exp i(\omega - i\alpha)t = \hat{p} \cdot \exp(i \cdot a \cdot k \cdot t) \qquad (63)$$

where k is related to the frequency of oscillations ($\omega = 2\pi f$) and to the coefficient α characterizing amplification or damping.

Mechanisms considered in the acoustic balance assessment will either amplify the initial mode perturbation (combustion, turbulent flow) or will tend to damp it (nozzle, two-phase flow, mechanical vibrations).

Consequently, various terms are summarized which form coefficient α and express the contribution of each mechanism i:

$$\alpha = \sum_i \alpha_i$$

Detail of linear acoustic balance terms

(a) Gain resulting from pressure-coupling

This is written as follows:

$$\alpha_{cP} = \frac{\bar{a}}{2} \frac{\int_S \gamma \cdot M_b \cdot R \cdot \hat{p}_n^2 \cdot dS}{\int_V \hat{p}_2 \cdot dV} \tag{64}$$

where:

R = real part of the pressure-coupled propellant response;
M_b = Mach number of the gases leaving the burning surface;
$\hat{p}_n$ = shape of mode n (acoustic calculations).

Integrals are computed over the whole propellant burning surface S (numerator) and the whole chamber volume V (denominator).

(b) Gain resulting from velocity-coupling

Culick expresses the gain resulting from velocity-coupling, in the linear range, as follows:

$$\alpha_{cV} = \frac{\bar{a}}{2} \frac{\int_S R_v \cdot \hat{p}_n \cdot \nabla \hat{p}_n \cdot dS}{\int_V \hat{p}_n^2 \cdot dV} \tag{65}$$

where R_v is the imaginary part of the propellant velocity-coupled response.

(c) Gain resulting from the average flow rate and its perturbations (vortex shedding)

Especially devoted to segmented configurations (propellant grains independently mounted in a motor), Brown *et al.*'s research [63] shows the nature of interactions between flow and acoustic fields. Vortices detach from the aft end of one segment and impact on the following downstream segment. A perturbation travels back through along the flow and can reinforce vortex shedding effects. These experiments performed in cold gas channels revealed the importance of Strouhal number S_t, defined as:

$$S_t = \frac{f \cdot d}{\bar{u}}$$

where:

f = vortex shedding frequency;
d = characteristic distance;
$\bar{u}$ = average flow velocity.

These experiments have demonstrated that coupling between chamber acoustics and flowfield occurs when $0.2 < S_t < 1$. This law seems to be correctly proven on actual rocket motors. The formulation of this contribution to acoustic balance has yet to be properly expressed and verified.

(d) Particulate damping

Because of their dynamic and thermal drags, particles distributed in gases induce attenuation and dispersion of the pressure waves in the combustion chamber. Culick [64] proposed the following expression describing the damping capacity of spherical particles of diameter d:

$$\alpha_p = -\frac{1}{2} \frac{C_m}{1 + C_m} \left[\frac{\omega^2 \cdot \tau_d}{1 + \omega^2 \cdot \tau_d^2} + (\gamma - 1) \frac{c_s}{c_g} \frac{\omega^2 \cdot \tau_t}{1 + \omega^2 \cdot \tau_t^2} \right] \tag{66}$$

where $\tau_d = \rho_s \cdot d^2 / 18\,\mu$ and $\tau_t = (3/2)\,(c_s/c_g)\,P_r \cdot \tau_d$

are, respectively, the dynamic and thermal relaxation times, and

ω = pulsation;
C_m = particles mass ratio;
ρ_s, c_s = respectively, density and specific heat of the particles;
μ, γ, c_g = respectively, viscosity, specific heat ratio and gas specific heat at constant pressure;
d = particles diameter;
P_r = Prandtl number.

A very detailed knowledge of the particle size distribution in the combustion chamber remains one of the main difficulties in making an accurate particulate damping prediction. At present, calculations are done only on rough estimations of this particle size distribution.

(e) Losses associated with nozzle impedance

These are written as follows:

$$\alpha_t = -\frac{\bar{a}}{2}\frac{\int_S (A_t + M_e)\hat{p}_n^2 \cdot dS}{\int_V \hat{p}_n^2 \cdot dV} \tag{67}$$

where:

M_e = Mach number in the nozzle entrance plane;
A_t = admittance of the nozzle in the same plane. The absolute value of the upper integral is computed over this reference plane; the absolute value of the denominator is calculated for the whole chamber volume.

With longitudinal modes and short nozzles (entrance cone length ≪ wavelength) and assuming isentropic oscillations, we have:

$$A_t = \frac{\gamma - 1}{2} \cdot M_e$$

In complex cases the nozzle admittance is numerically calculated.

(f) Visco-acoustic losses

The initial linear acoustic balance model does not take into account viscous phenomena, which are of primary importance for the particles behavior and appear close to the burning surface.

Culick suggested introducing the so-called "flow turning" effect for the first time in 1973. Flandro's approach [65] is based on a detailed analysis of the fluid layer located near the burning surface. His method uses the notion of admittance correction. Both approaches give very similar results when used for simple propellant grains under strong flow conditions.

(g) Losses caused by the solid grain

This contribution requires additional calculation: the acoustic analysis of the cavity is coupled with a vibration analysis of the propellant grain. At the gas/solid interface, displacements are set to the same value, so that continuity is ensured. Using experimental results for the propellant complex modulus it becomes possible to evaluate structural damping.

4.3.4.3. The second step: evaluation of oscillation amplitudes and average pressure shifts—non-linear analyses

There are two kinds of approach:

- Exact methods, which strive to solve complete equations, are using numerical procedures that are, at this time, very difficult to apply to actual motors [66,67].
- Approximate methods which simplify the problem: the system of partial derivative equations representing the motor operation is cast into a differential equations system. This approach, proposed by Culick [68], is the so-called "averaging" method, which has been successfully applied to rocket motors with simple geometry.

4.3.5. Longitudinal instabilities

4.3.5.1. First step: linear acoustic balance

(a) Characterization of the propellant pressure-coupled response

Indirect Methods

These methods are based on the propellant response determination from a model and on the unsteady analysis of a test motor firing. Two types of motors are widely used: self-excited or pulsed center-vented burners and rotary valve or modulated exhaust burners.

T-Burner. The T-burner (Fig. 23) is a tube at the end of which two propellant samples are placed (end-burning slabs or small slotted tubes) [64].

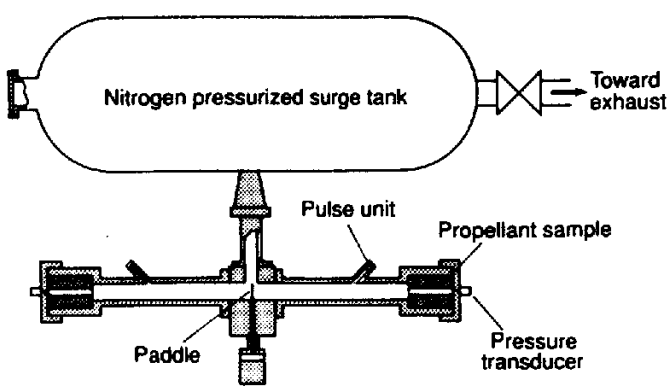

FIG. 4.23. T-burner schematic of the set-up.

The frequency is determined by T-length and average gas temperature. The combustion products are flushed outside through a non-sonic center vent toward a surge tank which maintains the T-average pressure roughly constant during firing. The whole set-up is nitrogen pressurized before firing in order to simulate the actual motor operating pressure. Various longitudinal modes can be observed:

- self-excited operation mode: the term corresponding to pressure oscillations increase, α_1, is determined during firing, and after burn-out the α_2 term related to damping phenomena becomes available.
- pulsed operation mode: pressure oscillations are triggered during firing by pulsers. They allow determination of the α_i terms describing the rate of amplitude change of the driven oscillations. The difference $\alpha_c = \alpha_1 - \alpha_2$ gives the combustion contribution related to the propellant pressure-coupled response.
- Variable area T-burner: in this mode, obtained by using hollow cylindrical sample with variable combustion area, the T-burner may exhibit oscillations even with highly aluminized compositions.

ONERA modulated exhaust motor [69]. In his technique (PEM burner), oscillations are driven in the combustion chamber during the whole firing. The test motor includes an end-burning propellant grain, and a nozzle limited to its entrance cone. A cog-wheel rotates in front of the throat area, producing a partial modulation of the throat nozzle area and of the ejected flow.

The propellant response is obtained by analyzing the pressure oscillations, the throat modulation oscillations, and using an operational model of the test motor. Figure 24 shows the pressure-coupled response of a propellant tested in the SNPE T-burner and ONERA PEM motor.

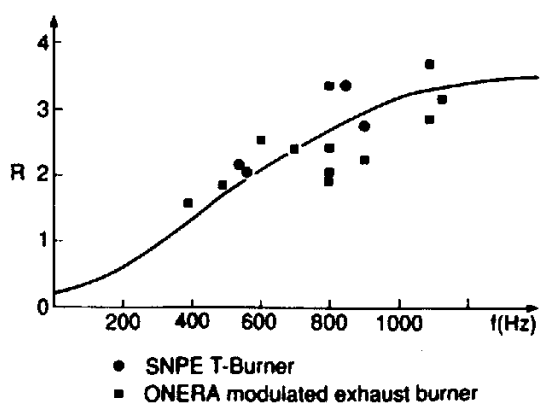

FIG. 4.24. Propellant pressure-coupled responses measured with modulated exhaust and center-vented burners.

Direct methods

Results obtained with the previous indirect methods are not very accurate. This lack of accuracy is mainly related to model deficiencies as well as to technical difficulties involved in test implementation.

To overcome these difficulties, studies have been undertaken in the United States [70] and in France (at ONERA) in order to directly determine fluctuations of specific mass flow rate induced by transient pressure fluctuations. Fluctuation measurements in this case are based on the analysis of the changes in the characteristics of a microwave frequency electrical wave traveling through the propellant and reflecting on the burning surface.

(b) Velocity-coupling characterization

This is a delicate determination because of the difficulties met in designing a test device in which the propellant would be affected only by acoustic velocity oscillations. This phenomenon being always associated with pressure-coupling, the intricate aspect of this characterization is enhanced by the fact that the velocity-coupled response is very closely linked to internal aerodynamics. It is necessary to make sure that the considered testing device gives a valid reproduction of the internal flowfield pattern of the actual motor.

(c) Linear acoustic balance assessment

Philippe and Tchepidjian [71] have developed a computer code based on an analysis of linearized equations which performs the acoustic balance for axisymmetrical motors. The input data are the parameters related to the pressure coupling α_c, average flow rate α_e, nozzle impedance α_t, particulate α_p, and structural vibrations.

Parametric studies performed with this code demonstrate that the most significant terms correspond to pressure-coupling and particulate damping. In order to account for experimental discrepancies and simplified assumptions (in particular, particle size distribution), the authors have defined the following criteria:

- damping of considered acoustic mode when $\alpha \leq -0.1\,f$;
- occurrence of the considered acoustic mode when $\alpha \geq +0.1\,f$;
- "critical" acoustic mode when $-0.1\,f < \alpha < 0.1\,f$.

4.3.5.2. Second step: non-linear aspect—limiting amplitudes and average pressure shifts

Test results are obtained by firing star-shaped grains with a constant burning area. When half of the web is burned, an impulse is triggered by

igniting a load of black powder located at the front-end of the propellant. Under low average pressures, pressure oscillations damp: the rocket motor is in a steady configuration. Under higher average pressures the pressure perturbation grows and reaches a limiting cycle. In this case the chamber average pressure is most of the time largely increased.

Tests performed at various pressures allow the determination of a threshold pressure p_s. Applied to a large number of polyurethane and polybutadiene propellants [72], they help to draw a pressure-burning rate diagram in which pressure thresholds are located along a line that separates steady and unsteady regions (Fig. 25).

This is a useful test for the classification of various compositions according to their instability tendencies from a non-linear point of view. It is also used to characterize the motor sensitivity to high-amplitude pressure and velocity perturbations.

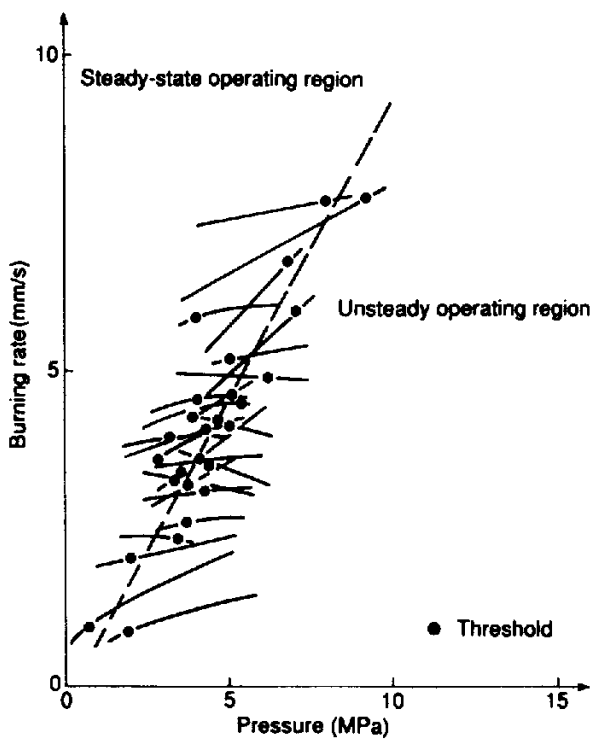

FIG. 4.25. Determination of steady-state and unsteady regions in a velocity versus pressure plot.

4.3.6. *Transverse instabilities*

4.3.6.1. *Experimental studies*

Firings exhibiting transverse instabilities (generally tangential) are characterized by high-frequency pressure oscillations and significant average pressure shifts.

A special burner equipped with a viewing port has been designed in order to observe combustion phenomena. The pressure level in the cylindrical combustion chamber is recorded at several locations in one cross-section. Tests performed demonstrate that the observed acoustic modes are unsteady modes. Furthermore, random motions of nodal lines are observed: strong rotations correspond with high pressure peaks.

4.3.6.2. *"L/D" Method*

At the origin of this method, a series of investigations [72] have been done on simple grain geometries, and researchers varied the firing conditions to determine an acceptable operation range (Fig. 26). They proposed a non-linear criterion to compare the severity of the observed acoustic modes. This criterion is defined as the ratio of the amplitude of the first pressure shift (Δp) to the stabilized pressure level p just before the shift. The motor operation is said to be steady when $\Delta p/p$ is zero or small (a few per cent) and unsteady when $\Delta p/p$ is high (several tens of per cent). It is a non-linear criterion.

(a) Effect of burning to throat area ratio K

With a given propellant, it can be noticed that pressure oscillations are first driven by K growth. Then these oscillations rapidly diminish, becoming non-existent beyond a threshold value K_s (or threshold pressure p_s).

(b) Effect of length

While keeping a constant K value, increase of the propellant grain length (without varying its port section) leads to unsteady effects beyond a threshold length L_s.

(c) Effect of initial diameter

By varying the propellant grain length for different values of the initial diameter, we observe:

- The existence of an L/D threshold, beyond which pressure oscillations occur. This threshold value varies from 5 to 10 depending on the propellant composition.

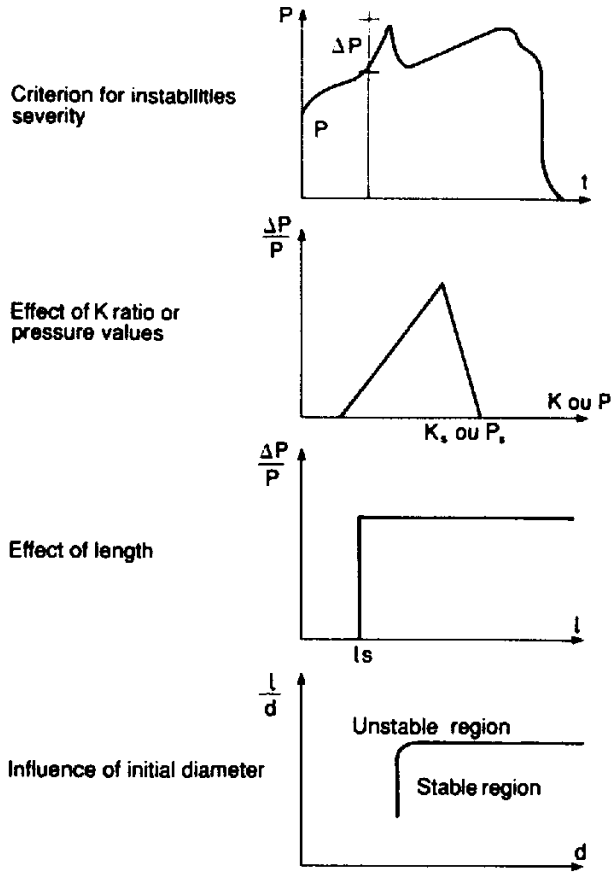

FIG. 4.26. Research of a steady-state operation range.

- In some cases the existence of a critical diameter, below which motor firings are always instability-free.

4.3.6.3. *Acoustic balance*

Few studies have been done on this method in the field of transverse instabilities, because of the lack of experimental evaluation for the propellant response function at these high frequencies.

Lovine [74] has described a slotted T-burner. Its small dimensions make it possible to obtain frequencies up to 13 kHz. Kuentzmann *et al.* [75] have developed a motor with a partially modulated nozzle throat. Response measurements between 3 and 15 kHz are obtained within one firing, which is due to the geometrical evolution of the propellant grain.

4.3.7. *Suppression of instabilities*

There are two ways to cancel instabilities:

- the first consists of adjusting the propellant grain shape;
- the other consists of tailoring the propellant (production of particles that damp oscillations during combustion).

Implementation of these solutions is never easy. The solutions require design testing, and improvements are always obtained at motor performance expense.

4.3.7.1. *Propellant grain geometry*

(a) Helmholtz resonator

This is a small cavity linked to the combustion chamber through a throat. It must be located at a vibrational antinode and tuned to the frequency that needs to be damped. This device has been used several times to stabilize longitudinal modes.

(b) Resonance rod

This device is widely used. It consists of a rod embedded at the forward end of a rocket motor; it fills a portion of the central port length. Rods with rectangular or cruciform sections are the most efficient. They prevent gas rotation and suppress pressure peaks, particularly at the beginning of firing.

(c) Longitudinal baffles

These are small plates placed lengthwise inside the propellant grain. During combustion, they emerge inside the combustion chamber and create obstacles that block the rotation of the gases.

4.3.7.2. *Propellant composition*

The addition of a low particle content, as ingredients in the propellant, is a method often successful in stabilizing motor combustion. This is particularly true in the case of tangential instabilities. Once the frequency that needs to be damped is known, it is possible to theoretically predict, depending on the particulate nature, the most efficient particle diameter [76]. This first estimation is very helpful in selecting size distribution of commercial products.

The actual problem is in fact much more complex, because there is often not one frequency, but a large frequency range that needs to be stabilized, and

the products used never exhibit a single diameter. Aluminum has been used for quite a long time; because of the lack of control on the alumina particles diameter that are produced in the combustion gases it is impossible to reach a maximum damping. Therefore, researchers have made new attempts with inert products, the high melting point of which gives the possibility of damping effect optimization with low particle amounts. This solution has the additional advantage of not affecting the rocket motor signature.

With an average particle size ranging from 1 to 2 μm, these products provide good damping for frequencies of the order of 15 kHz.

Bibliography

1. CHRISTENSEN, W. N., Development of an acoustic emission strand burning technique for motor burning rate prediction. AIAA 78-984, AIAA/SAE/ASME, 14th Joint Propulsion Conference, 1978.
2. TRAINEAU, J. C. and KUENTZMANN, P., Some measurements of solid propellant burning rates in nozzleless motors. AIAA 84-1469, AIAA/SAE/ASME, 20th Joint Propulsion Conference, 1984.
3. KUBOTA, N., OHLEMILLER, T. J., CAVENY, L. H. and SUMMERFIELD, M., The mechanism of super-rate burning of catalysed double-base propellants. AIAA 74-124, AIAA/SAE/ASME, 10th Joint Propulsion Conference, 1974.
4. LENGELLÉ, G. *et al.*, Steady-state burning of homogeneous propellant. *Fundamentals of Solid Propellant Combustion*, Vol. 90, Progress in Astronautics and Aeronautics, pp. 361-403, 1984.
5. LENGELLÉ, G., Thermal degradation kinetics and surface pyrolysis of vinyl polymers, *AIAA Journal*, **8**, 1989-1996, November 1979.
6. KUO, K. K., *Principles of Combustion*. Wiley Interscience, 1986.
7. WILLIAMS, F. A., *Combustion Theory*. Addison-Wesley, 1965.
8. BECKSTEAD, M. W., DERR, R. L. and PRICE, C. F., A model of composite solid propellant combustion based on multiple flames, *AIAA Journal*, **8**(12), 2200-2207, 1970.
9. ZENIN, A. A., Structure of temperature distribution in steady-state burning of a ballistic powder, *Combustion, Explosion and Shock Waves*, **2**(3), 1966.
10. WILLIAMS, F. A., BARRERE, M. and HUANG, M. C., *Fundamental Aspects of Solid Propellant Rockets*, Agardograph 116, Technivision, 1969.
11. AOKI, Y. H. and KUBOTA, N., Combustion wave structures of high and low energy double-base propellants. AIAA 80-1165, AIAA/SAE/ASME, 16th Joint Propulsion Conference, 1980.
12. BECKSTEAD, M. W., Model for double-base propellant combustion. AIAA 80-4079, AIAA/SAE/ASME, 16th Joint Propulsion Conference, 1980.
13. KING, M. K., A model for prediction of effects of pressure, cross-flow velocity and heat of explosion on double-base propellant burning rate. AIAA 81-1555, AIAA/SAE/ASME, 17th Joint Propulsion Conference, 1981.
14. COHEN, N. S., Analysis of double-base combustion. AIAA 81-0120, AIAA/SAE/ASME, 17th Joint Propulsion Conference, 1981.
15. FERREIRA, J. G., BIZOT, A. and LENGELLÉ, G., Model for double-base propellants combustion, with and without additives. AIAA 83-1197, AIAA/SAE/ASME, 19th Joint Propulsion Conference, 1983.
16. KISHORE, K., PAI VERNECKER, V. R. and KRISHNA-MOHAN, V., Differential scanning calorimetric studies on ammonium perchlorate, *Thermochimica Acta*, 13, 277-292, 1975.
17. SELEZNEV, V. A., POLHIL, P. F., MALTSEV, V. M. and BAVYKIN, I. B., An optical method of measuring the burning surface temperature of condensed systems, *Combustion and Flame*, 13(2), 139-142, 1969.
18. GUIRAO, C. and WILLIAMS, F. A., A model for ammonium perchlorate deflagration between 20 and 100 Atm, *AIAA Journal*, **9**(7), 1345-1356, 1971.

19. BOGGS, T. L., The thermal behavior of cyclotrimethylene trinitramine (RDX) and cyclotetramethylene tetranitramine (HMX) *Fundamentals of Solid Propellant Combustion*, Vol. 90, Progress in Astronautics and Aeronautics, pp. 121-168, 1984.
20. FIFER, R. A., Chemistry of nitrate ester and nitramine propellants, *Fundamentals of Solid Propellant Combustion*, Vol. **90**, Progress in Astronautics and Aeronautics, pp. 177-225, 1984.
21. BOGGS, T. L., PRICE, C. F., ZURN, D. E., DERR, R. L. and DIBBLE, E. J., The self-deflagration of cyclotetramethylene tetranitramine (HMX). AIAA 77-859, AIAA/SAE/ASME, 13th Joint Propulsion Conference, 1977.
22. RAMOHALLI, K. N. R., Steady-state burning of composite propellants under zero cross-flow situation, *Fundamentals of Solid Propellant Combustion*, Vol. 90, Progress in Astronautics and Aeronautics, pp. 409-472, 1984.
23. GODON, J. C., Modélisation de la combustion normale et érosive des propergols composites. Thèse de Docteur d'Etat es-sciences physiques, Université Pierre et Marie Curie, Paris 6ème, Soutenue le 24 novembre 1983.
24. MESSNER, A. M., Transient coning in end-burning solid propellant grains. AIAA 80-1138, AIAA/SAE/ASME, 16th Joint Propulsion Conference, 1980.
25. SMITH, R. E., End burning technology program: interim report. Task A: laboratory effort. Task B: subscale motor tests. Aerojet Solid Propulsion Company, Sacramento, Calif., Report AFRPL-TR-71-38, AD-891 362, October 1971.
26. JOLLEY, W. H., HOOPER, J. F., HILTON, P. R. and BRADFIELD, W. A., Studies on coning in end-burning rocket motors, *Journal of Propulsion*, **2**(3), 223-227, 1986.
27. BRONGNIART, C., DAMIEN, M. and FRÈCHE, A., Chargements propulsifs à combustion frontale a forte vitesse de combustion, mis en oeuvre par le procédé Epictète (Casting process). ICT, *International Jahrestagung, Technologie des Poudres et Explosifs, Karlsruhe*, pp. 361-374, 1984.
28. FRIEDLANDER, M. P., III and JORDAN, F. W., Radial variation of burning rate in center perforated grains. AIAA 84-1442, AIAA/SAE/ASME, 20th Joint Propulsion Conference, 1984.
29. BECKMAN, C. W. and GEISLER, R. L., Ballistic anomaly trends in subscale solid rocket motors. AIAA 82-1092, AIAA/SAE/ASME, 20th Joint Propulsion Conference, 1984.
30. KALLMEYER, T. E. and SAYER, L. H., Differences between actual and predicted pressure-time histories of solid rocket motors. AIAA 82-1094, AIAA/SAE, ASME, 18th Joint Propulsion Conference, 1982.
31. BOGGS, T. L., ZURN, D. E. and DERR, R. L., The effects of strain on the burning rates of high energy solid propellants. 13th JANNAF Combustion Meeting, September 1976.
32. PLANTIF, B., Influence of acceleration on the combustion of solid propellants, measurement and prediction of the effects. *Problems and Methods of Simulation of the Environment*. ICT Jahrestagung, Karlsruhe, pp. 409-451, 1972.
33. BOISSON, J., *La propulsion par fusée*. Cours de l'Ecole Nationale Supérieure des Techniques Avancées, Vol. 1, 2, 1981.
34. DELANNOY, G., Prediction of antitank solid propellant rockets internal ballistics. AIAA 84-1355, AIAA/SAE/ASME, 20th Joint Propulsion Conference, 1984.
35. YANENKO, N. N., *The Method of Fractional Steps*. Springer-Verlag, Berlin, Heidelberg, New York, 1971.
36. GODOUNOV, S., ZABRODINE, A., IVANOV, M., KRAIKO, A. and PROKOPOV, G., *Résolution numérique des problèmes multidimensionnels de la dynamique des gaz*, Editions Mir-Moscou, 1976.
37. ASCH, G., CHARNAY, G. and SCHON, J. P., Capteurs de vitesse, débit et niveaux de fluide. *Les capteurs en instrumentation industrielle*, Dunod, pp. 535-572, 1982.
38. RAZDAN, M. K. and KUO, K. K., Erosive burning. *Fundamentals of Solid Propellant Combustion*, Vol. 90, Progress in Astronautics and Aeronautics, pp. 515-592, 1984.
39. KING, M. K., Erosive burning of composite solid propellants: experimental and modeling studies. AIAA 78-979, AIAA/SAE/ASME, 14th Joint Propulsion Conference, 1978.
40. MARKLUND, T. and LAKE, A., Experimental investigation of propellant erosion, *ARS Journal*, 3, 173-178, February 1960.
41. BARRÈRE, M. and LARUE, P., Contribution à l'étude de la combustion érosive des poudres composites, *La Recherches Aérospatiale*, No. 95, pp. 25-36, July August 1963.

42. LENOIR, J. M. and ROBILLARD, G., A mathematical method to predict the effect of erosive burning in solid propellant rocket. *Sixth International Symposium on Combustion*, Reinhold Publishing Co., pp. 663-667, 1957.
43. LENGELLÉ, G., Model describing the erosive combustion and velocity response of composite propellants, *AIAA Journal*, **13**(3), 315-322, March 1975.
44. KING, M. K., A model of the erosive burning of composite propellants. AIAA 77-930, AIAA/SAE/ASME, 13th Joint Propulsion Conference, 1977.
45. BEDDINI, R. A., Analysis of injection-induced flows in porous walled ducts with application to the aerothermochemistry of solid propellant motors. Thesis of the Graduate School of Rutgers, New Jersey, October 1981. See also BEDDINI, R. A., Injection induced flows in porous-walled ducts, *AIAA Journal*, **24**(11), pp. 1766-1773, 1986.
46. KUO, K. K., GORE, J. P. and SUMMERFIELD, M., Transient burning, *Fundamentals of Solid Propellant Combustion*, **90**, 599-653, 1984.
47. KRIER, H., T'IEN, J. S., SIRIGNANO, W. A. and SUMMERFIELD, M., Non-steady burning phenomena of solid propellants: theory and experiments, *AIAA Journal*, **6**(2), 278-285, 1968.
48. KRIER, H., Solid propellant burning rate during a pressure transient, *Combustion Science and Technology*, **5**, 69-73, 1972.
49. SUMMERFIELD, M., CAVENY, L. H., BATTISTA, R. A., KUBOTA, N., GOSTINTSEV, YA. and ISODA, H., Theory of dynamic extinguishment of solid propellants with special reference to non-steady heat feed-back law, *Journal of Spacecraft and Rockets*, **8**(3), 251-258, 1971.
50. DE LUCA, L., GALFETTI, L., RIVA, G. and TOBACCO, U., Unstable burning of thin solid propellant flames. AIAA 80-1126, AIAA/SAE/ASME, 16th Joint Propulsion Conference, 1980.
51. SUMMERFIELD, M. and PARKER, K. H., Interrelations between combustion phenomena and mechanical properties in solid propellant rocket motors; mechanics and chemistry of solid propellants. *Proceedings of the 4th Symposium on Naval Structural Mechanics*, Pergamon Press, pp. 75-116, 1967.
52. BARRÈRE, M., L'allumage des propergols solides, Considérations générales, *La Recherche Aérospatiale*, No. 123, pp. 15-28, March-April 1968.
53. HERMANCE, C. E., Solid propellant ignition theories and experiments, *Fundamentals of Solid Propellant Combustion*, Vol 90, Progress in Astronautics and Aeronautics, pp. 239-295, 1984.
54. LENGELLÉ, G., MENTRÉ, P. G., GUERNIGOU, J., BIZOT, A. and MAISONNEUVE, Y., Allumage et extinction des propergols solides. Paper submitted at the 53rd Symposium of the AGARD Commission "Propulsion et Energétique sur la Technologie des moteurs fusées à propergols solides", OSLO, 2-6 April 1979.
55. DE LUCA, L., Solid propellant ignition and other unsteady combustion phenomena induced by radiation. Ph.D. thesis, Dept. of Aerospace and Mechanical Sciences, Princeton University, N.J. AMS Rept 1192-T, November 1976.
56. GUERNIGOU, J., INDRIGO, C., MAISONNEUVE, Y. and MENTRÉ, P. G., Mise au point de fluxmètre à température superficielle, *La Recherche Aérospatiale*, No. 3, pp. 159-168, 1980.
57. DE LUCA, L., CAVENY, L. H., OHLEMILLER, T. J. and SUMMERFIELD, M., Radiative ignition of double-base propellants, I — Some formulation effects, *AIAA Journal*, **14**(7), pp. 940-946, July 1976.
58. OHLEMILLER, T. J., CAVENY, L. H., DE LUCA, L. and SUMMEFIELD, M., Dynamic effects on ignitability limits of solid propellants subjected to radiative heating. Contract AFOSR-69-1651-BRL, *14th International Symposium on Combustion*, Combustion Institute, Pittsburgh, Pa. pp. 1297-1307, 1973.
59. DE LUCA, L., Extinction theories and experiments, *Fundamentals of Solid Propellant Combustion*, Vol. 90, Progress in Astronautics and Aeronautics, pp. 661-726, 1984.
60. FLEMING, R. W. and DERR, R. L., The use of non-reactive coatings in solid propellant arc-image ignition studies. *Proceedings of the 7th JANNAF Combustion Meeting*, CPIA Publication 204, Vol. 1, pp. 379-389, 1971.
61. CULICK, F. E. C., A review of calculations for unsteady burning of solid propellant, *AIAA Journal*, **6**(12), pp. 2241-2255, 1968.
62. CULICK, F. E. C., Stability of high-frequency pressure oscillations in rocket combustion chambers, *AIAA Journal*, **1**(5), pp. 1097-1104, May 1963.
63. BROWN, R. S., DUNLAP, R., YOUNG, S. W. and WAUGH, R. C., Vortex shedding as an additional source of acoustic energy in segmented solid propellant rocket motors. AIAA 80-1092, AIAA/SAE/ASME 16th Joint Propulsion Conference, 1980.

64. CULICK, F. E. C. (Editor), T-Burner testing of metallized solid propellants. AFRPL-TR-74-28, 1974.
65. FLANDRO, G. A., Solid propellant acoustic admittance corrections, *Journal of Sound and Vibrations*, **36**, pp. 297-312, 1974.
66. KOOKER, D. E. and ZINN, B. T., Numerical solution of axial instabilities in solid propellant rocket motors, *10th JANNAF Combustion Meeting*, CPIA Publication 243, Vol. I, pp. 389-415, 1973.
67. KUENTZMANN, P., Etudes récentes à l'ONERA sur les instabilités de combustion dans les moteurs fusées à propergol solide. AGARD CPP No. 259, Solid Rocket Motor Technology, 1979.
68. CULICK, F. E. C., Non-linear behavior of acoustic waves in combustion chamber, *Acta Astronautica*, **3**, 715-757, 1976.
69. KUENTZMANN, P. and NADAUD, L., Réponse des propergols solides aux oscillations de pression et de vitesse, *Combustion Science and Technology*, **11**, 119-139, 1975.
70. STRAND, L. D., SCHULTZ, A. L. and REEDY, G. K., Microwave Doppler shift technique for determining solid propellant transient regression rates, *Journal of Spacecraft and Rockets*, **11**, 75-83, February 1974.
71. PHILIPPE, A. and TCHEPIDJIAN, P., Prediction of longitudinal combustion instabilities in axisymmetrical propellant grains. AIAA 84-1358, AIAA/SAE/ASME, 20th Joint Propulsion Conference, 1984.
72. TISSIER, J. P. and LHUILLIER, J. N., Etude récentes des instabilités de combustion dans les fusées à propergol solide. *Colloque sur la combustion des propergols solides*, Poitiers, 1972, Cahiers de la Thermique, No. 4, Série B, pp. 35-40, May 1974.
73. BROWNLEE, N. G. and MARBLE, P. B., An experimental investigation in solid propellant rocket motors. Solid Propellant Rocket Research Conference, ARS Paper 1067, 1960.
74. LOVINE, R. H., High frequency propellant response measurements. AIAA 77-976, AIAA/SAE/ASME, 13th Joint Propulsion Conference, 1977.
75. KUENTZMANN, P. and LAVERDANT, A., Détermination expérimentale de la réponse d'un propergol solide aux oscillations de pression de haute fréquence, *La Recherche Aérospatiale*, No. 1, pp. 39-55, 1984.
76. EVANS, G. I. and SMITH, P. K., The suppression of combustion instability by particulate damping in smokeless solid propellant motors, AGARD CPP No. 259, *Solid Rocket Motor Technology*, pp. 27.1-27.10, 1979.